THE INFLUENCE OF PHENOCRYSTS IN SILICIC MAGMA DEGASSING

By

Rebecca deGraffenried, B.S.

A Thesis Submitted in Partial Fulfillment of the Requirements

For the Degree of

Master of Science

in

Geology

University of Alaska Fairbanks

August 2017

Approved:

Jessica Larsen, Committee Chair
Jeffrey Freymueller, Committee Member
Pavel Izbekov, Committee Member
Paul McCarthy, Chair *Department of Geosciences*
Paul Layer, Dean *College of Natural Science &*
Mathematics
Michael Castellini, *Dean of the Graduate School*

Abstract

Understanding the degassing process in magma is an important goal because of the first-order control it exerts on determining eruption style. Degassing in high viscosity magmas is of particular interest since these magmas tend to erupt explosively. However, the role of phenocrysts in the degassing process is still poorly constrained, though recent data indicate that the presence of phenocrysts should promote permeability development at lower porosities than in crystal-free magmas. This study specifically examined the effect of phenocrysts in a rhyolitic magma, but the results can also be applied to crystal-rich intermediate magmas that have rhyolitic matrix melts. Isothermal decompression experiments were conducted using powdered rhyolite (76 wt. % SiO_2) and seeded with corundum (Al_2O_3) crystals to approximate magmas with 20 and 40 vol. % phenocrysts. Experiments were saturated at 900°C and 110 MPa then continuously decompressed to final pressures between 75 and 15 MPa. Percolation threshold was determined by measuring permeability on a benchtop permeameter and measuring porosity from reflected light images. Additionally, vesicle structure was assessed by measuring pore throat radii from back-scattered electron images and plotting bubble size distributions. Finally, degassing state was checked by measuring dissolved water contents in the glass with Fourier Transform Infrared (FTIR) spectroscopy analyses. The addition of at least 20 vol. % phenocrysts resulted in a decrease in percolation threshold from 70-80 vol. % porosity in crystal-free rhyolites to 55 vol. % porosity. Bubble size distribution patterns indicate that coalescence was more widespread as final pressure decreased and crystal content increased. Minimum pore throat radii in the 40 vol. % phenocryst series were larger than in the 20 vol.% phenocryst and crystal-free series. The dissolved water measurements indicate that these experiments degassed in equilibrium even at the fast decompression rate of 0.25 MPa/s. Calculations of the magnitude of

outgassing from the decreased percolation threshold and timescales of pressure dissipation indicate that the presence of phenocrysts plays a role in the effusive-explosive cyclicity of Vulcanian-style eruptions.

Table of Contents

List of Figures

List of Tables

x

Acknowledgements

This work would not have been possible without the excellent guidance and mentorship of my advisor, Jessica Larsen, and the insight of my other committee members, Jeff Freymueller and Pavel Izbekov. Many thanks also go out to my friends and family, whose support helped me through the challenging times. This work was funded by the National Science Foundation. Portions of this work were performed at the Advanced Instrumentation Laboratory at the University of Alaska Fairbanks, and some of the images were produced at the High-Resolution X-ray Computed Tomography Facility of the University of Texas at Austin.

1.0 Introduction

Silicic volcanism ($SiO_2 \geq 57\%$, spanning andesitic to rhyolitic composition) presents a distinct hazard to human life. These compositions tend to produce explosive eruptions, ranging in style from Plinian to sub-Plinian to Vulcanian (Cashman and Sparks, 2013). These explosive eruptions result from the high viscosity of these melts, which, along with slow H_2O diffusion rates, kinetically hinders degassing processes compared to mafic compositions. High melt viscosity and slow diffusivity hinders bubble nucleation and growth, promotes volatile supersaturation, and results in significant overpressure development within the melt (Gardner et al., 2000). Additionally, it has been suggested that the significant supersaturation of volatiles can result in a late-stage bubble nucleation event that drives fragmentation and explosive eruptions specifically in rhyolites (Mangan and Sisson, 2000). However, silicic magmas can also erupt effusively or transition between explosive and effusive eruption styles, such as during the 1980 eruption of Mt. St. Helens in the Cascades range of the western USA; this eruption transitioned through Plinian and Vulcanian eruptions to effusive dome building over the course of several months (Cashman and McConnell, 2005). Various factors can influence degassing processes to produce transitioning eruptions, such as ascent rate, permeability of the conduit, volatile content, and crystallization during ascent (Jaupart and Allegre, 1991; Cashman and McConnell, 2005; Diller et al., 2006). Because so many factors can influence the chemistry and physics of degassing, many studies have been performed on both natural and experimental samples to understand the degassing process (e.g., Gardner et al., 2000; Larsen and Gardner, 2000; Burgisser and Gardner, 2004; Larsen et al., 2004; Wright et al., 2009; Yokoyama and Takeuchi, 2009; Lindoo et al., 2016). The experimental work has mostly examined crystal-free systems in order to understand basic processes involved in degassing, such as bubble nucleation, growth,

coalescence, and magma ascent rate (Gardner et al., 1999; Gardner et al., 2000; Larsen et al., 2004; Castro et al., 2012a; Lindoo et al., 2016). However, many natural magmas contain a significant amount of crystals (>10 vol. %) either as phenocrysts or microlites. Many of the experimental studies have noted that the presence of crystals could influence the degassing process but little experimental work has been done to try to constrain that influence (e.g., Gardner et al., 1999). Only one study has experimentally examined the role of crystals (Okumura et al., 2012) seeded into rhyolite melts, so more experimental work is necessary. Therefore, the goal of this study was to determine whether euhedral phenocrysts (355 μm) influence the degassing process in high-silica melts and if so, what volume percent was necessary to produce the influence. Results indicate that the presence of at least 20 vol. % phenocrysts leads to bubble connectivity and permeability development and lower porosities, indicating crystal-rich melts could degas deeper in the conduit than crystal-free melts.

2.0 Background

Once an eruption has been triggered, magma begins ascending from the magma chamber to the surface through the conduit. As the magma ascends, the overlying pressure is decreased, thus decreasing the solubility of volatiles. However, due to surface tension and viscosity, bubbles do not immediately nucleate; a certain degree of supersaturation is necessary for nucleation to occur (Mangan and Sisson, 2000). The degree of supersaturation necessary is dependent upon the melt composition and whether nucleation is homogeneous or heterogeneous. Homogeneous nucleation occurs when bubbles nucleate in free space and requires a large amount of supersaturation. Experiments have indicated that it could take up to 150-200 MPa of supersaturation in rhyolites for homogeneous nucleation to occur (Mangan and Sisson, 2000). Heterogeneous nucleation occurs when bubbles nucleate on a pre-existing surface, such as a

crystal. The efficacy of heterogeneous nucleation depends upon the type of crystal present as well as the magma composition. For example, in rhyolitic magmas, bubbles nucleate well on Fe-Ti oxides but poorly on plagioclase (Hurwitz and Navon, 1994). On the other hand, in dacitic magmas, bubbles do not nucleate well on Fe-Ti oxides (Mangan et al., 2004). The wetting angle between the melt, bubble, and crystal surface determines how well bubbles will nucleate. If the wetting angle is acute, this indicates that the melt adheres strongly to the crystal surface, which does not leave a large enough surface area for the gas to adhere to the crystal; thus, nucleation will not be favored on that crystal type in that magma composition (Hurwitz and Navon, 1994; Mangan et al., 2004). A schematic representation of this relationship is shown in Figure 1. If heterogeneous nucleation can occur efficiently, it has been shown to drop the necessary supersaturation down to only 5 MPa (Hurwitz and Navon, 1994). Another key component to bubble nucleation is forming a stable nucleus. Because of surface tension, a certain minimum radius, termed the critical radius, is necessary for bubbles to be stable. Until bubbles grow to this critical radius, they are unstable and may collapse.
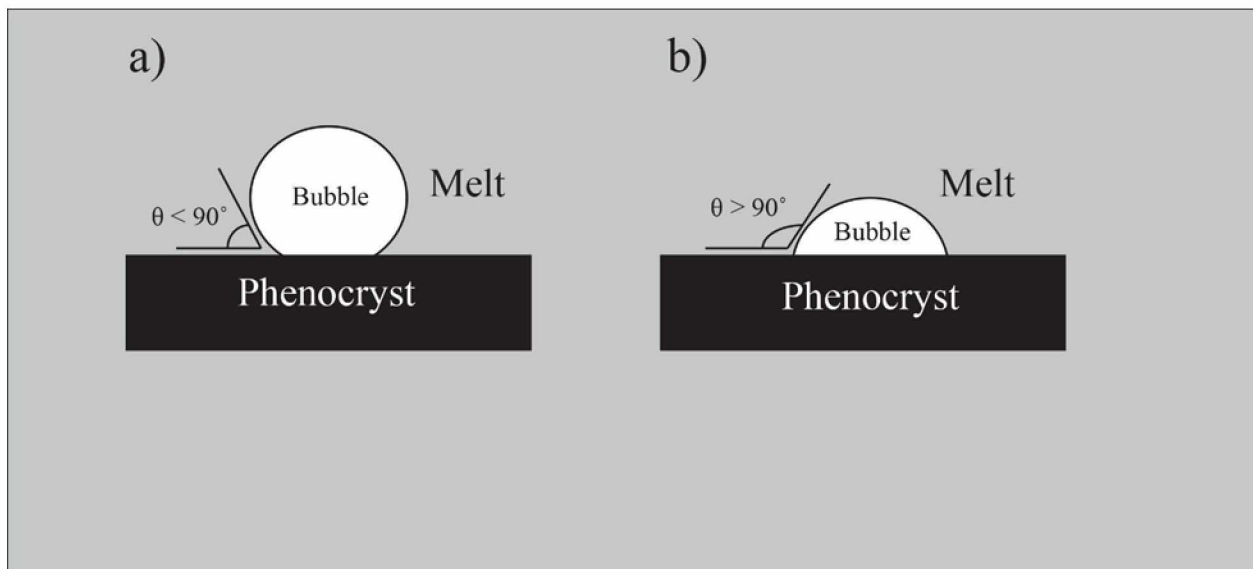
Figure 1. Schematic representation of wetting angle. In case a) the melt strongly wets the crystal and nucleation is not favored. In case b) the melt does not strongly wet the crystal and nucleation is favored.

Once stable bubble nuclei have been formed, any decrease in overlying pressure from magma ascent will result in bubble growth. Bubbles grow by two main mechanisms – diffusion of volatiles into pre-existing bubbles and decompression-triggered expansion. Both processes are impeded by the high viscosity of high silica melts. Bubble growth by diffusion is controlled by the diffusivity of the volatiles, which can range from 10^{-11} m^2/s for an andesite (Behrens et al., 2004) to 10^{-12} m^2/s for a rhyolite (Zhang and Behrens, 2000). Diffusivity is also a function of melt viscosity; the higher the viscosity, the more difficult it becomes for volatiles to diffuse through the melt. The viscosity of water saturated, crystal-free intermediate and felsic magmas can range from 10^2 Pa s for an andesite (Vetere et al., 2006) to 10^5 Pa s for a rhyolite (Hess and Dingwell, 1996). The values for these viscosities will increase as the magma decompresses, loses its volatiles, and crystallizes. Additionally, there is a limited distance that the water can travel within the degassing time period. Thus there is a water-depleted shell around the bubbles from water diffusing into bubbles. The size of this shell is dependent on the size of the bubble and the diffusivity of the water in the melt. Bubbles will also grow by gas expansion as the overlying pressure decreases. As a magma ascends, the confining pressure decreases and the volatiles already within the bubbles will expand according to the ideal gas law. However, in order to expand, bubbles must move magma out of the way, which is challenging when the viscosity is high (Gardner et al., 2000).

When the bubbles have grown sufficiently large, they begin to impinge on one another. This causes deformation of the bubbles and eventually coalescence. Pervasive coalescence leads to magma permeability, and the porosity at which this occurs is termed the percolation threshold (Φ_c; Blower, 2001). There are two main mechanisms for bubble coalescence – drainage of melt from the melt film between the bubbles and stretching of the melt film from bubble growth

(Castro et al., 2012a). In rhyolitic melts, melt drainage has been estimated to take 10^4 to 10^9 seconds, whereas coalescence by film stretching can take 10^1 to 10^3 seconds, depending upon bubble size (Castro et al., 2012a; Nguyen et al., 2013). Based on these time scales, the most likely mechanism for bubble coalescence in high viscosity melts is stretching of the melt film resulting from bubble growth. Coalescence can also be induced by shear stress (Okumura et al., 2008; Caricchi et al., 2011). Most commonly, magmas will experience shear stress along the conduit walls (Okumura et al., 2008). However, the shear stress from the conduit walls only has a local effect on magma along the edges and, depending on the conduit radius, does not affect the magma located in the center of the conduit (Castro et al., 2012b). When two bubbles coalesce, the aperture that forms between the bubbles is termed the pore throat. The size of this aperture is an important property for determining the permeability of a melt as the smallest pore throat will restrict the permeability of the whole sample (Yokoyama and Takeuchi, 2009).

Once permeability has been established, gas can begin to escape from the magma, either vertically through the column of permeable magma or horizontally through the conduit walls (Jaupart and Allegre, 1991; Diller et al., 2006). Vertical escape out the vent is only possible if the path is not blocked by an impermeable lava plug (e.g., as in a Vulcanian eruption) or if vertical variations in permeability do not significantly impede gas escape. Horizontal gas escape is controlled by the permeability of the conduit wall rocks (Jaupart and Allegre, 1991). The conduit wall rocks can be permeable to start with or become permeable as an eruption causes fractures to form in the conduit wall rocks. Evidence for the second process can be seen from boreholes that intersected the conduit beneath the Inyo Domes in California (Heiken et al., 1988). Conversely, as an eruption proceeds, the permeability of the conduit wall rocks can decrease through hydrothermal precipitation of quartz, particularly in cases where the magma is hydrous

(Edmonds et al., 2003). Thus, magma outgassing can be a function of both changes in magma permeability and changes in conduit wall rock permeability, which in turn will influence eruption style.

The relationship between permeability and porosity has typically been explored through the context of two different models, the Kozeny-Carman relationship and percolation theory (e.g., Blower, 2001; Rust and Cashman, 2004). The Kozeny-Carman relationship relates permeability (k) to porosity (Φ) and pore geometry:

$$k = \frac{\Phi a^2}{C} \tag{1}$$

where a is the average hydraulic radius of pore throats and C is a geometrical constant, typically 2 for cylinders (e.g., Saar and Manga, 1999). This relationship implies that permeability is strongly dependent on the size of pore throats. Other studies have confirmed that pore throat size, rather than bubble size, controls permeability (Saar and Manga, 1999; Klug et al., 2002; Rust and Cashman, 2004).

Percolation theory predicts a power-law relationship between permeability and porosity of the form:

$$k = c(\Phi - \Phi_c)^b \tag{2}$$

where c is a constant that determines permeability magnitude and the exponent b is controlled by the percolation pathway geometry, typically 2 for infinite cylinders and 3 for infinite cracks (Sahimi, 1994). When modelling vesicles as overlapping spheres, percolation theory predicts Φ_c = 30 vol. % porosity (Blower, 2001). However, many natural and experimental crystal-free samples (rhyolite and rhyodacite composition) do not show measurable permeabilities until a

6

threshold of at least 56 vol. % is reached (Eichelberger et al., 1986). However, most studies indicate that the critical porosity is much higher, between 70 and 80 vol. % porosity (Klug and Cashman, 1996; Takeuchi et al., 2009; Lindoo et al., 2016). Analogue experiments conducted by Oppenheimer et al. (2015) indicate that a certain threshold of phenocrysts could decrease the percolation threshold in highly silicic magmas by restricting bubble growth pathways as the system approaches a state of random loose packing of the crystals. At this point, the rheology of the system develops yield strength. The crystal-restricted vesiculation process evolves as bubbles elongate away from crystal surfaces, impinge on one another, and coalesce earlier in the degassing process than in a crystal-free magma, thus allowing the magma to develop permeability at a lower porosity. However, experimental studies investigating the relationship between crystal content and percolation threshold have had differing results. Lindoo et al. (2015) found that the addition of >20 vol. % crystals to phonolites resulted in a reduction of the percolation threshold from 75 vol. % to 53 vol. % porosity. On the contrary, Okumura et al. (2012) found no measurable permeability in experiments with up to 50 vol. % phenocrysts and measured porosity up to 61 vol. %. Thus, a big question remains as to whether and to what extent phenocrysts influence the degassing process.

Since the number of experimental studies is so few and have conflicting results, this study aims to investigate the role phenocrysts play in the degassing process in order to provide a better constraint. This study used decompression experiments with corundum seed crystals to approximate phenocrysts and powdered rhyolite obsidian to investigate the role phenocrysts play specifically in high viscosity melts. Results from permeability and porosity measurements show that experiments with ≥20 vol. % phenocrysts become measurably permeable at a lower porosity (55 vol. %) than crystal-free rhyolites (70-80 vol. %). The mechanism proposed by Oppenheimer

et al. (2015), crystals inducing coalescence by restricting bubble growth pathways, appears to be the reason for this decrease in percolation threshold. Calculations of outgassing from the decreased percolation threshold relative to a crystal-free melt indicate that significant outgassing can occur if gas can escape either vertically through the permeable column of magma or horizontally into permeable conduit walls. These results have implications for effusive-explosive eruption transitions, particularly in the context of Vulcanian eruptions.

3.0 Methods

3.1 Experimental methods

The decompression experiments employed powdered rhyolite obsidian from Mono Craters, CA (Table 1) and euhedral corundum seed crystals sieved to 355 μm to approximate phenocrysts with relatively low aspect ratios (AR) and equant shapes (AR: 1.8 ±0.6, n=64, range: 1.1-3.5). Two different experimental series were conducted – 20 and 40 vol. % corundum seed populations. Two crystal-free experiments were conducted as control experiments in order to compare to Lindoo et al. (2016) results. One other crystal free experiment was conducted to assess the proportion of porosity contributed from hydration bubbles, which resulted from water being trapped in spaces between powder grains (Gardner et al., 1999; Larsen and Gardner, 2000). The total volume of powder and corundum was 0.053 cm^3, which corresponded to ~0.0833 g of corundum and 0.0713 g of powder for the 40 vol. % series and 0.0416 g of corundum and 0.0951 g of powder for the 20 vol. % series. The only exceptions were the two highest quench pressure 40 vol. % series experiments (P$_f$= 65 and 50 MPa) which had a total volume of 0.065 cm^3, corresponding to 0.1021 g of corundum and 0.0875 g of powder. For experiments quenched at higher pressures (P$_f$ ≥ 30 MPa), approximately 7 wt. % water was added, and for experiments quenched at lower pressures (P$_f$ ≤ 25 MPa), approximately 5 wt. % water was added (Table 2).

8

Table 1. Major oxide composition of Mono Craters rhyolite[a]

Oxide	Percentage
SiO_2	76.32 (0.29)
TiO_2	0.21 (0.17)
Al_2O_3	13.02 (0.06)
FeO*	1.03 (0.8)
MgO	0.04 (0.02)
CaO	0.53 (0.03)
Na_2O	3.93 (0.11)
K_2O	4.72 (0.1)
Total	100
n[b]	4

[a]Values from Lindoo et al. (2016). 1σ standard deviations given in parentheses

[b]Number of analyses

The amount of added water was decreased for the lower quench pressure experiments in order to reduce the chance of capsules bursting during decompression. Both amounts were enough to reach the saturation value (4.15 wt. %) calculated from the solubility model of Moore et al. (1998). The starting materials and water were sealed in 5 mm silver (Ag) tubing using a PUK 3 arc welder. Smaller capsules of MgO powder in 4 mm diameter Ag tubing were sealed in the headspace of the capsules to act as a sink for excess water vapor produced during decompression (Figure 2). The capsules were checked for leaks by weighing the capsules before and after welding as well as after allowing the capsule to sit on a hot plate at 150°C for 15 minutes. If the weight changed during either check, the capsule was discarded.

Once a satisfactory capsule was produced, the capsule was loaded into a TZM (Ti-Zr-Mo alloy) pressure vessel. The pressure vessel was fitted with a water-cooled cold seal top that allowed for a rapid quench so that bubble textures at the end of the decompression would be preserved with minimal cooling-induced expansion (Figure 3). Approximately 2.5 bars of CH_4

9
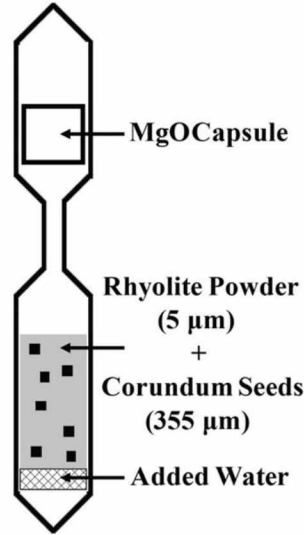
Figure 2. Schematic diagram of capsule design. Not to scale.

gas was added to the vessel in order to prevent H diffusion out of the capsules. The vessel was

pressurized with Ar gas to 110 MPa and heated to 900°C in a vertical Deltech furnace. Pressure

in the system was measured using a Heise gauge accurate to ±5 MPa, according to the

manufacturer's specifications for the University of Alaska Fairbanks (UAF) gauge. The

experiments were held at the initial conditions for 24 hours, long enough to allow the water to

diffuse into the center of the largest powder grains. This timescale can be estimated from the

equation (Larsen and Gardner, 2004):

$$L = \sqrt{Dt} \qquad (3)$$

where L is length, D is water diffusivity, and t is time. Diffusivity is calculated from Nowak and

Behrens (1997), and at 110 MPa, 4.15 wt. % water, and 900°C, the diffusivity is 36.7 μm^2/s. At a

hold time of 24 hours, the water can diffuse 5×10^5 μm, which is a larger distance by many orders

of magnitude than any possible grain size of powder. One experiment was also checked using

Fourier Transform Infrared (FTIR) spectroscopy to ascertain that the water was diffusing

uniformly through the experiment.

Table 2. Experiment starting materials

Sample	Mass powder (g)	Vol. % powder	Mass Al_2O_3	Vol. % Al_2O_3	Wt. % H_2O	Initial mass (g)	Final mass (g)	Mass change[a]	Wt. % H_2O lost
MCO-NEQ-6	0.1142	100.00	0	0.00	6.92	0.9640	0.9640	0.0000	0.00
MCO-TCM-1	0.0870	59.85	0.1022	40.15	7.03	1.8022	1.8001	-0.0021	1.11
MCO-TCM-2	0.0869	59.17	0.1050	40.83	7.19	1.6243	1.6187	-0.0056	2.92
MCO-TCM-4	0.0709	60.08	0.0825	39.92	7.04	1.6341	1.6304	-0.0037	2.41
MCO-TCM-5	0.0950	80.00	0.0416	20.00	6.88	1.6648	1.6651	0.0003	0.00
MCO-TCM-6	0.0948	80.12	0.0412	19.88	7.35	1.5464	1.5518	0.0054	0.00
MCO-TCM-12	0.0957	80.34	0.0410	19.66	6.95	1.6873	1.6848	-0.0025	1.83
MCO-TCM-13	0.0711	60.26	0.0821	39.74	7.57	1.6802	1.6756	-0.0046	3.00
MCO-TCM-14	0.0960	80.16	0.0416	19.84	7.27	1.6217	1.6194	-0.0023	1.67
MCO-TCM-17	0.0715	60.11	0.0831	39.89	5.17	1.5863	1.5828	-0.0035	2.26
MCO-TCM-20	0.0955	80.12	0.0415	19.88	5.18	1.3151	1.3153	0.0002	0.00
MCO-TCM-22	0.0950	79.84	0.0420	20.16	5.18	1.3989	1.3982	-0.0007	0.51
MCO-TCM-26	0.0955	79.81	0.0423	20.19	5.29	1.6371	1.6351	-0.0020	1.45
MCO-TCM-27	0.0713	59.90	0.0836	40.10	4.97	1.5154	1.5119	-0.0035	2.26
MCO-TNCM-4	0.1191	100.00	0.0000	0.00	7.22	1.5355	1.5354	-0.0001	0.08
MCO-TNCM-7	0.1052	100.00	0.0000	0.00	7.32	1.6987	1.6980	-0.0007	0.67

[a] Positive mass changes are a result of graphite powder from inside the pressure vessel clinging to the capsule

At the end of the hold period, the experiments were decompressed continuously and isothermally at a rate of 0.25 ±0.03 MPa/s to final pressures between 75 and 15 MPa by carefully bleeding pressure from a leak valve and timing with a stopwatch. Once the desired final pressure was reached, the pressure vessel was lifted from the furnace and quickly flipped so that the capsule fell to the water-cooled head space. All samples were quenched within 10 seconds of reaching the desired final pressure, and this hold time was incorporated into calculations of actual decompression rate.
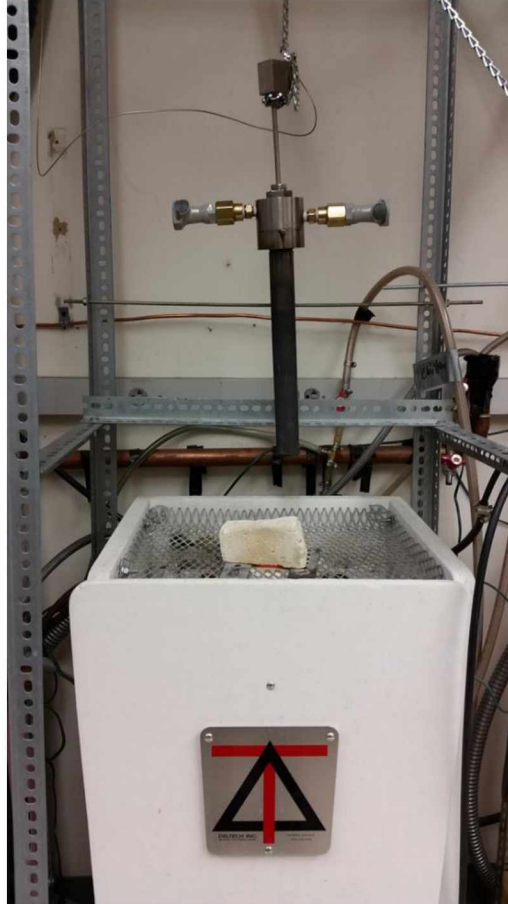
Figure 3. Example of experimental set up. Water hoses attach to the top of the pressure vessel and provide the cooling method for rapidly quenching samples. Experiment capsule is located at the bottom of the vessel.

3.2 Analytical methods

Once the capsule was removed from the pressure vessel, the experiment was carefully extracted from the tubing using wire cutters and a razor blade. The samples were prepared for analyses of porosity, permeability, vesicle structure, and three-dimensional computed x-ray tomography using a variety of different methods according to analytical procedure, as follows.

3.3 Permeability

Samples were prepared for permeability measurements first by being wrapped by Crystalbond 509 then submerged in Hillquist epoxy and allowed to cure overnight. The shell of

Crystalbond 509 was necessary to prevent the less viscous Hillquist epoxy from permeating the sample during the curing period. The resulting epoxy pucks were cut and polished such that both ends of the sample were suitably exposed and the thickness of the sample was at least five times the diameter of the largest bubble (Blower, 2001). Permeability measurements were conducted on a benchtop permeameter located at the University of Alaska Fairbanks that was designed after Takeuchi et al. (2008) specifically for the small experimental samples. Compressed air, regulated by a precision CKD pressure regulator to between 0.005 and 0.1 MPa, was passed through the sample, which created a pressure differential between the upstream and downstream sides of the variably permeable or impermeable samples. This pressure differential was measured with a Testo 526 digital manometer. The gas flow through the sample was measured with an Omega FMA 4308 digital mass flow meter with accuracy of ±1% of full scale and a range of 0 to 500 mL/min. One sample (MCO-TCM-27) had a low enough flow rate through the sample (<5 mL/min) that a flow rate converter was used to convert the gas flow to water flow so that a more accurate measurement could be made. The flow rate converter worked by directing the downstream air flow into a tube of water, and the air bubbles forced out an equivalent volume of water. The expelled water was caught and weighed on an electric scale, and using the density of water, the volumetric flow rate of the air was calculated. Permeability was determined by measuring at least 10 different gas flow rates and resulting pressure differentials, which create a curve that can be fit using a second-order polynomial. The polynomial curve fit was then used to estimate permeability coefficients using the Forchheimer equation (Figure 4):

$$\frac{P_2^2 - P_1^2}{2P_0 L} = \frac{\mu}{k_1} v + \frac{\rho}{k_2} v^2 \tag{4}$$

where P_2 and P_1 are the pressures at the top and bottom of the sample, respectively, P_0 is the pressure of the fluid at which fluid viscosity (μ) and velocity (v) are measured, typically defined as $P_0 = P_1$, L is sample length, ρ is fluid density, k_1 is Darcian permeability and k_2 is inertial permeability (Rust and Cashman, 2004). The Forchheimer equation is preferable to the classic Darcy's law since it incorporates inertial permeability, which arises from turbulent flow through the permeable bubble pathways.
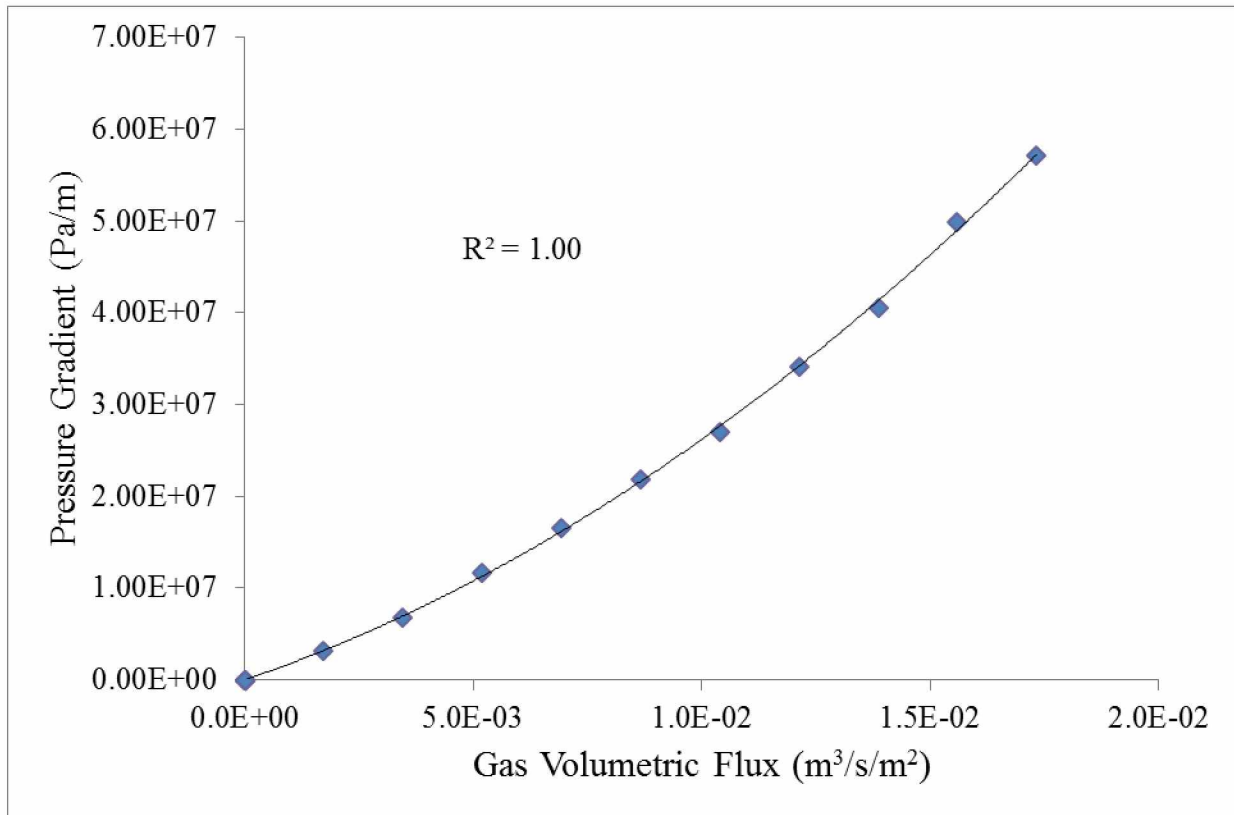
Figure 4. An example of a fit of the second order polynomial to the Forchheimer Equation. This example is for MCO-TCM-4, and the correlation coefficient R^2 indicates a nearly perfect fit to the second order polynomial curve used to obtain values of k_1 (viscous) and k_2 (inertial) permeabilities.

3.4 X-ray tomography

After the permeability measurements were conducted, a subset of the experimental samples was soaked in acetone to dissolve the Crystalbond shell and allow for removal of the experiments from the epoxy puck. 3D X-ray computed tomography images of five experiments

were obtained from the University of Texas at Austin High Resolution X-ray Computed Tomography Facility. Two samples from each crystal series were sent, one permeable and one impermeable, as well as one impermeable crystal-free sample from this study and one permeable crystal-free sample from Lindoo et al. (2016). Samples that were sent for tomography are denoted in Table 3 with an asterisk. The images had a resolution of 5 microns/voxel.

3.5 Porosity

Porosities of the samples were measured using stereology from reflected light images taken with a Nikon DS-Fil camera attached to an Ortholux II POL-BK petrographic microscope. Samples were polished flat by hand using silicon carbide powder and the finishing polish was conducted using 1 micron diamond grit until the surface was reflective. Images of the samples were taken only using a 20x lens due to shadows created by the difference in reflectivity between the glass and the corundum seeds in lower magnification images. Five to ten images of each sample were taken and then analyzed using NIH ImageJ. The images were converted to binaries using thresholding, creating black bubble areas and white glass and crystal areas. Following the rules of stereology, any bubbles on the edges of the images were excluded (Russ, 1986). However, where a coalesced set of bubbles was on the edge, the edge of the bubble completely within the area of the image was manually separated from the edge bubble. The area of any crystals in the images was subtracted so that the reported porosity represents the porosity of the melt only. Figure 5 shows an example of a reflected light image and the resulting segmented binary image. Porosity for MCO-TCM-4 and MCO-TCM-12 was measured with the same method but using a tomography image slice instead of a reflected light image. The tomography images could not be used to measure porosity for the higher quench pressure experiments since the voxel resolution of the tomography images resulted in loss of all bubbles

15

Table 3. Summary of experimental conditions

Sample	Vol. % Crystals	Temperature (°C)	Initial P (MPa)	Quench P (MPa)	Decompression time (s)	Decompression Rate (MPa/s)
MCO-NEQ-6	0	900	110	110	n/a	n/a
MCO-TCM-5	20	900	110	75	140	0.25
MCO-TCM-1	40	900	110	65	180	0.25
MCO-TCM-6*	20	900	110	50	260	0.23
MCO-TCM-2*	40	900	110	50	250	0.24
MCO-TCM-14	20	900	110	30	350	0.23
MCO-TCM-13	40	900	110	30	320	0.25
MCO-TNCM-4	0	900	110	25	390	0.22
MCO-TCM-12*	20	900	110	25	360	0.24
MCO-TCM-20	20	900	110	25	348	0.24
MCO-TCM-22	20	900	110	25	345	0.25
MCO-TCM-4*	40	900	110	25	390	0.22
MCO-TCM-27	40	900	110	25	320	0.27
MCO-TNCM-7*	0	900	110	20	370	0.24
MCO-TCM-26	20	900	110	15	383	0.25
MCO-TCM-17	40	900	110	15	390	0.24

* Experiments that were sent for tomography

<5 μm in diameter. In the higher quench pressure experiments (Pf $\geq$50 MPa), that bubble size made up a significant portion of the porosity. Error in the porosity measurement was estimated by creating a stitch map of MCO-TCM-5. Images of the entire surface of the sample were taken with at least 40% overlap between each image, and Adobe Photoshop was used to stitch the images together. The resulting image was analyzed three times following the method described above, and the standard deviation between the three measurements is the reported error.
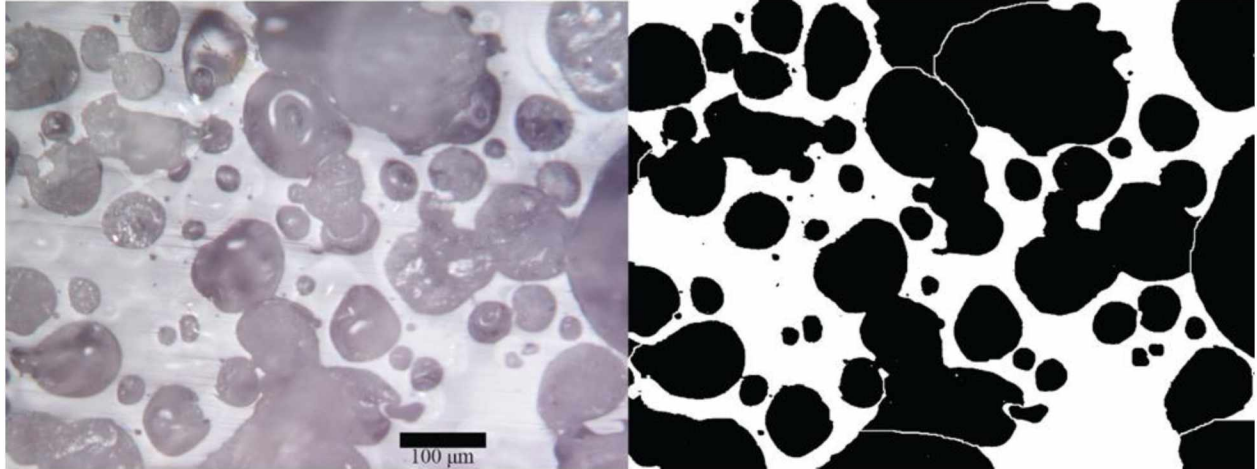
Figure 5. Reflected light image and corresponding binary segmented image. The scale is the same for both images, and the image comes from MCO-TCM-14.

3.6 Vesicle characterization

Vesicle size distributions were determined by calculating the radius of a circle of equivalent area from bubble areas determined in the porosity measurements. One representative sample from each crystal series and quench pressure was analyzed. The bin size for the histograms was determined using geometric series (Proussevitch and Sahagian, 1998; Shea et al., 2010) by starting with the largest bubble radius size from all the samples (830 µm; MCO-TCM-4) and multiplying by a factor of 0.67. Each resulting bubble size was multiplied by the same factor until the final category was 1.4 µm. The use of this ratio is more statistically accurate and resulted in sufficient divisions between bubble sizes such that changes in bubble size trends were apparent without resorting to an unnecessary number of divisions (Shea et al., 2010). The number of bubble radii in each sample that fit the bin size were counted and plotted as a frequency histogram.

Pore throats of permeable samples were measured from back-scattered electron images captured on the Environmental Scanning Electron Microscope (ESEM) located in the University of Alaska Fairbanks' Advanced Instrumentation Laboratory. The ESEM was used since it

allowed these images to be taken without any polishing or coating necessary, and it produced images with a higher resolution than tomography (0.2 μm/pixel). Two permeable crystal-free samples from Lindoo et al. (2016; MC-27 and MC-31) were obtained, and the pore throats of these samples were also measured. Images were analyzed using NIH ImageJ by selecting the perimeter of the pore throat with the polygon selector tool so that the area of the pore throat was most accurately measured. Some pore throats were obscured by the shape of the bubbles or by glass debris from cutting the sample, so only completely exposed pore throats were measured. The area of the pore throat was measured and that area was converted to the radius of a circle with an equivalent area in order to normalize the effect from the differing shapes of the pore throats.

3.7 Dissolved water content

Samples were prepared for FTIR analysis by polishing both sides by hand using silicon carbide grit and 1 micron diamond grit finishing paste until the sample had a thickness of 25-100 microns and was highly reflective. The water contents were measured using a Thermo Fisher Scientific 6700 Fourier Transform Infrared Spectrometer paired with a Continuum microscope that has two liquid nitrogen-cooled MCT-A detectors, one standard and one with a small area detector that allows for signal optimization for apertures less than 50x50 microns in size. A purge collar contained around the microscope stage flows dry air across the sample and was used during all analyses in order to minimize atmospheric effects. Samples were placed on an NaCl disk for transmission spectra, which were collected over the wavenumber range of 6500-650 cm^{-1} with an aperture of 30x30 microns. The analyses were conducted with 512 scans at a resolution of 4 cm^{-1}. Each sample was measured at 4 or 5 different points, and background spectra were

collected after each point. Dissolved water concentration (C) was calculated from the Beer-Lambert law:

$$C = \frac{MA}{\rho t \varepsilon} \qquad (5)$$

where M is molar mass of the species being analyzed, A is the height of the absorbance peak of the species, ρ is the density of the glass, t is sample thickness, and ε is the molar absorptivity of the glass dependent on composition. Depending on the analysis, either the H_2O_t peak at 3570 cm^{-1} or the overtone peaks, OH$^-$ at 4500 cm^{-1} and H_2O_m at 5230 cm^{-1}, were measured. For the 3570 cm^{-1} peak, a molar absorptivity of 90 L mol^{-1} cm^{-1} was used (Hauri et al., 2002). For the 4500 cm^{-1} and 5230 cm^{-1} peaks, molar absorptivities of 1.42 and 1.75 L mol^{-1} cm^{-1}, respectively, were used (Okumura and Nakashima, 2005). Peak height was measured as the average of 4-6 height measurements around highest point of the peak, within ±12 cm^{-1} (King and Larsen, 2013; Lindoo et al., 2016). Glass density was calculated using the model of Lange and Carmichael (1990) using equilibrium-predicted water contents, the experimental temperature, and the composition of the Mono Craters rhyolite starting powder.

Thicknesses of the samples at the measurement points were determined using reflectance spectra. Samples were transferred from the NaCl disk to a reflective gold mirror (Tamic et al., 2001; Nichols and Wysoczanski, 2007). Reflectance spectra were collected over the same wavenumber range as the transmission spectra, and background reflectivity was collected off the gold mirror after each measurement. The spectra were collected over 512 scans with a resolution of 4 cm^{-1}. If the sample is sufficiently thin (<150 microns), the reflectance spectra will produce interference fringes which have a wavelength proportional to the thickness of the sample

(Nichols and Wysoczanski, 2007). Thus the thickness can be calculated with the following

equation:

$$t = \frac{m}{2n(v_2 - v_1)} \tag{6}$$

Where m is the number of fringes in a given wavenumber interval, n is the refractive index of the

glass, and (v_2-v_1) is the wavenumber interval. Only fringes in the 2700-2100 cm^{-1} wavenumber

range were considered since the wavelength of the fringes changes outside this interval

(Wysoczanski and Tani, 2006). The refractive index for rhyolitic glasses is 1.491 (King and

Larsen, 2013).

4.0 Results

4.1 Permeability and porosity

The porosity measurements follow the expected exponential increase in porosity with

decreasing quench pressure (Figure 6; Table 4). The error on the porosity measurements was

calculated to be ±0.5 vol. %, and this value was applied to all porosity measurements. The

porosities increase from 30.1 vol. % (P_f = 75 MPa) to 69.4 vol. % (P_f = 15 MPa) for the 20 vol.

% crystals series and from 16.7 vol. % (P_f = 65 MPa) to 69.3 vol. % (P_f = 15 MPa) for the 40

vol. % crystals series. Predicted equilibrium porosity based on water solubility can be calculated

from Gardner et al. (1999):

$$\Phi_M = \frac{\frac{\rho_M}{Z} V_W (w_O - w_F)}{1 + \left(\frac{\rho_M}{Z} V_W (w_O - w_F)\right)} \tag{7}$$

where ρ_M is melt density, Z is molecular weight of the gas species, V_w is the molar volume of

water at the final pressure, and w_O and w_F are the weight fractions of water at the original and

20

Table 4. Summary of results

Sample	Vol. % Crystals	Porosity (vol. %)	log k_1 (m^2)[a, b]	log k_2 (m)	Dissolved H_2O (wt. %)[c]	log η_{melt} (Pa s)	log η_{bulk} (Pa s)
MCO-NEQ-6	0	13.9	B.D.L.	B.D.L.	3.89 (0.3)	4.54	4.54
MCO-TCM-5	20	30.1	B.D.L.	B.D.L.	n.d.	4.94	5.38
MCO-TCM-1	40	16.7	B.D.L.	B.D.L.	n.d.	5.09	6.28
MCO-TCM-6	20	40.9	B.D.L.	B.D.L.	2.00 (0.7)	5.34	5.78
MCO-TCM-2	40	41.2	B.D.L.	B.D.L.	2.30 (0.2)	5.34	6.53
MCO-TCM-14	20	51.9	B.D.L.	B.D.L.	n.d.	5.79	6.23
MCO-TCM-13	40	51.9	B.D.L.	B.D.L.	1.40 (0.2)	5.79	6.98
MCO-TNCM-4	0	62.9	B.D.L.	B.D.L.	n.d.	5.95	5.95
MCO-TCM-12	20	62.2	-13.87 (0.47)	-12.33 (1.23)	n.d.	5.95	6.39
MCO-TCM-20	20	54.9	B.D.L.	B.D.L.	1.60 (0.1)	5.95	6.39
MCO-TCM-22	20	56.3	-13.42 (0.37)	-9.03 (0.66)	n.d.	5.95	6.39
MCO-TCM-4	40	57.1	-13.94 (0.06)	-11.14 (0.22)	n.d.	5.95	7.14
MCO-TCM-27	40	60.5	-14.00 (0.11)	-11.48 (0.09)	n.d.	5.95	7.14
MCO-TNCM-7	0	69.7	B.D.L.	B.D.L.	n.d.	6.13	6.13
MCO-TCM-26	20	69.4	-12.81 (0.12)	-9.72 (0.23)	n.d.	6.36	6.80
MCO-TCM-17	40	69.3	-13.02 (0.33)	-10.51 (0.28)	n.d.	6.36	7.55

[a] B.D.L means the measured permeability was below the detection limit of the laboratory permeameter

[b] 1σ standard deviations reported in parentheses

[c] n.d. means the sample was not measured with FTIR, so there is no data

final pressures, respectively. The porosity of the lower quench pressure samples ($P_f < 50$ MPa) are all at or very close to equilibrium, within error, but the higher quench pressure samples ($P_f \geq$ 50 MPa) tend to have a higher porosity than equilibrium would predict, regardless of crystal content, likely a result of hydration bubbles and experimental method. Since powder was used as starting material instead of a solid slab, hydration bubbles were present in the experiments, which contributed to the increased porosity relative to predicted equilibrium porosity in the higher quench pressure experiments ($P_f \geq 50$ MPa; Gardner et al., 1999; Larsen and Gardner, 2000). The hydration bubble population in these experiments was determined to be 13.9 vol. % from an experiment conducted at the initial starting conditions and quenched without

decompression. The measured porosity of MCO-NEQ-6 (13.9 vol. %) was subtracted from experiments quenched at $P_f \geq 50$ MPa since these experiments are more dominated by bubble nucleation and thus most affected by the excess in porosity produced by hydration bubbles and the small decompression at the start of the run. This correction brings the higher quench pressure samples very close to or on the equilibrium line (Figure 6).

Measured permeabilities (Equation 4) of the experiments changed as a function of decreasing quench pressure and increasing vesicularity in both the 20 and 40 vol. % crystals series (Table 4). Crystal-bearing experiments were generally impermeable at $P_f > 25$ MPa. One 20 vol. % experiment, MCO-TCM-20, was impermeable at $P_f = 25$ MPa, with a porosity of 54.9 vol. %. All the crystal-free experiments had permeabilities below the detection limit of the laboratory permeameter ($k_1 = 10^{-15}$ m^2) to quench pressures as low as 20 MPa. Once permeability was measurable, the experiments showed a minimum log permeability of $k_1 = -14.0$ and $k_2 = -11.48$ (MCO-TCM-27; $P_f = 25$ MPa) and a maximum log permeability of $k_1 = -12.81$ and $k_2 = -9.72$ (MCO-TCM-26; $P_f = 15$ MPa). Both k_1 and k_2 generally increase with decreasing quench pressure and with increasing porosity. The percolation threshold for both the 20 and 40 vol. % crystals series appears to lie between 54.9 vol. % porosity and 56.3 vol. % porosity, the difference between the impermeable experiment MCO-TCM-20 and permeable experiment MCO-TCM-22.
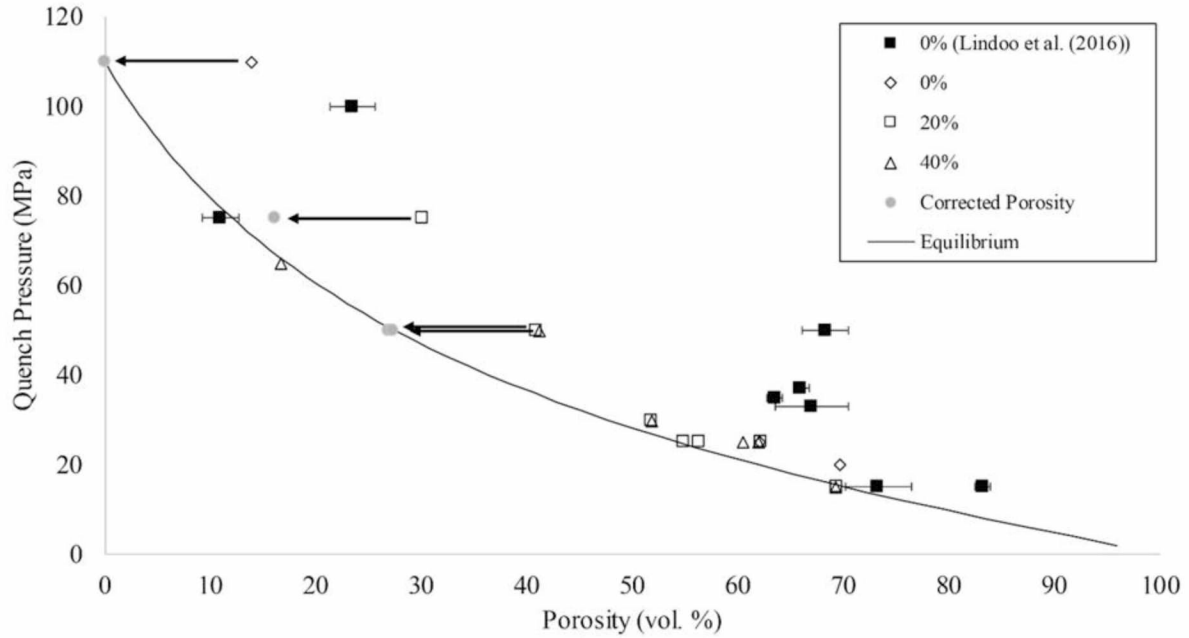
Figure 6. Plot of quench pressure versus measured porosity. The arrows indicate the 13.9 vol. % porosity from hydration bubbles and bubble nucleation that was subtracted from experiments in which these processes significantly impacted the measured porosity. Light grey circles represent the porosity values after the correction has been applied.

4.2 Vesicle structure

Bubble size distribution histograms are shown in Figure 7. The experiments which had their bubble size distributions determined from reflected light images have an arrow above the bar representing the smallest bubble size. This arrow indicates that there are more bubbles measured within that bubble size than shown in the frequency diagram. Many of the particles that were categorized as the smallest bubble size during the reflected light analysis were just single pixels that were missed during image analysis and thus do not represent actual bubbles. While these single pixels do not contribute significantly to the porosity since they do not contribute significantly to the measured bubble area, they skew the frequency diagram since the frequency diagram counts the number of them. Thus, the smallest bubble size bar was cut off in order to not misrepresent the actual distribution of bubbles present within the sample. For the samples which had porosity measured from the tomography images, the smallest diameter

bubble that could possibly be measured is 5 μm. This corresponds to a radius of 2.5 μm, which is larger than the two smallest bubble size divisions, so those two samples do not show any bubbles for that size division.
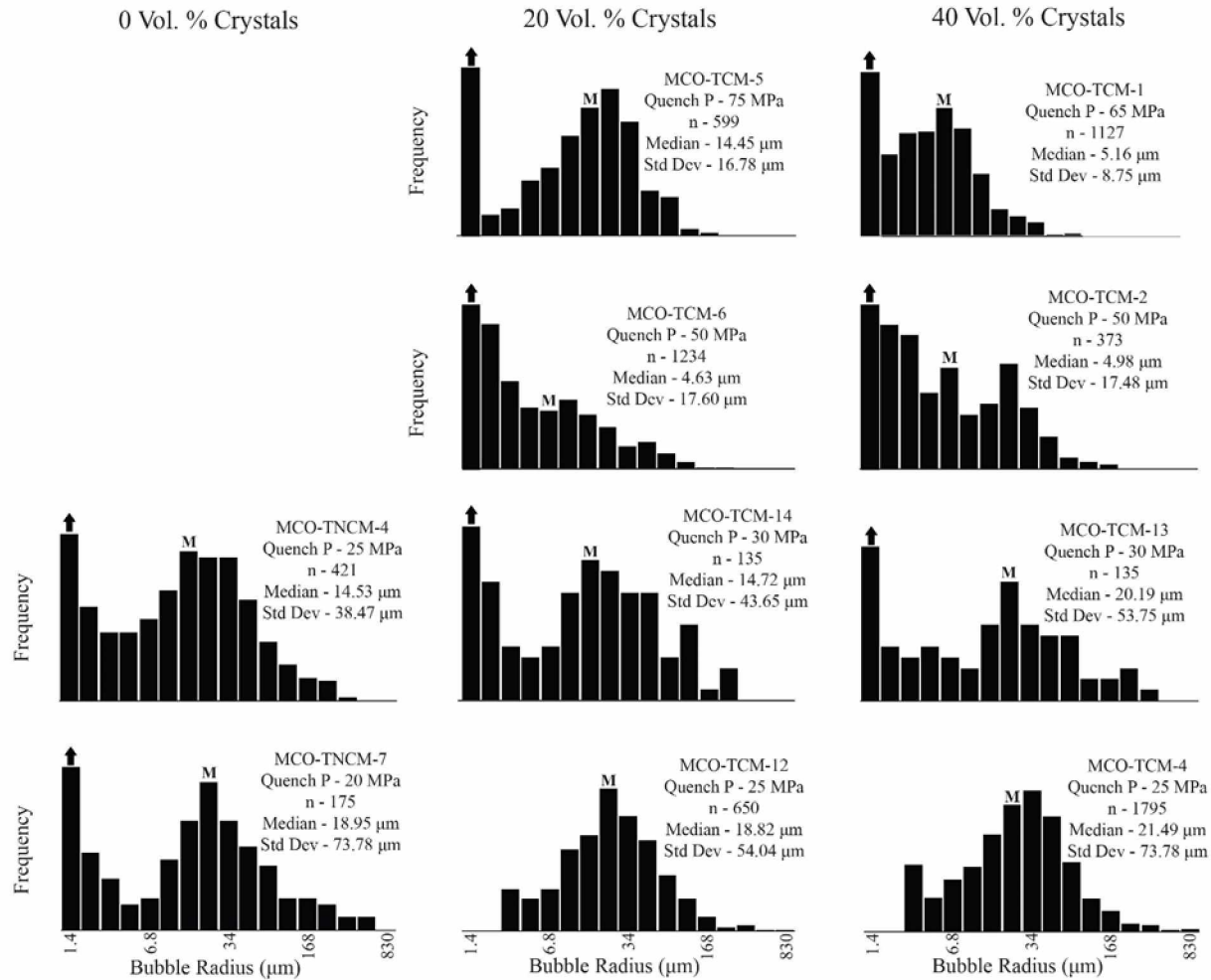
Figure 7. Frequency histograms of bubble sizes. The arrow above the smallest bubble size category indicates that there are more bubbles within that category that are not shown on the diagram. The "M" is above the bubble size category in which the calculated median bubble size is located.

Calculations of median bubble size and standard deviation excluded all bubbles in the smallest bubble size category. Ignoring the distributions of the two highest quench pressure experiments (MCO-TCM-5 and MCO-TCM-1) where hydration bubbles and bubble nucleation skew the plots, all three series show a shift of the median bubble radius peak to the right and the broadening of the peak as quench pressure decreases. The 40 vol. % series shows a shift from

median bubble radius at P_f = 50 MPa of 4.98 μm with a standard deviation of 17.48 μm to median bubble radius at P_f = 25 MPa of 21.49 μm with a standard deviation of 73.78 μm. The 20 vol. % series shows a shift from median bubble radius at P_f = 50 MPa of 4.63 μm with a standard deviation of 17.60 μm to median bubble radius at P_f = 25 MPa of 18.82 μm with a standard deviation of 54.04 μm. The two crystal-free experiments show a shift from median bubble radius at P_f = 25 MPa of 14.53 μm with a standard deviation of 38.47 μm to median bubble radius at P_f = 20 MPa of 18.95 μm with a standard deviation of 73.78 μm. At a quench pressure of 25 MPa, the 40 vol. % series showed the largest median bubble radius peak, likely a result of more extensive bubble coalescence forming larger bubbles.
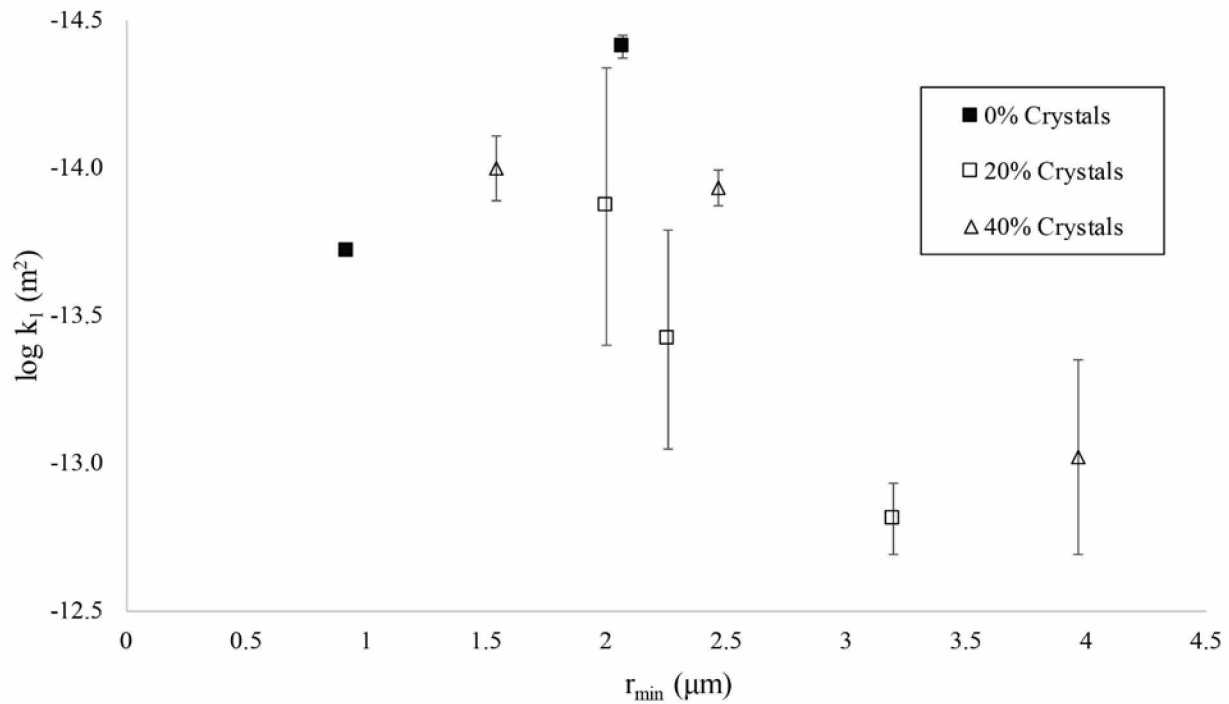
Figure 8. Plot of Darcian permeability versus minimum pore throat radius. The minimum pore throat radius tends to increase with increasing permeability and with increasing crystal content.

The minimum pore throat radius tended to increase with increasing permeability, as would be expected (Figure 8). The smallest pore throat was in MC-27 at a radius of 0.97 μm and the largest pore throat was in MC-31 at a radius of 123.52 μm (Table 5). The average
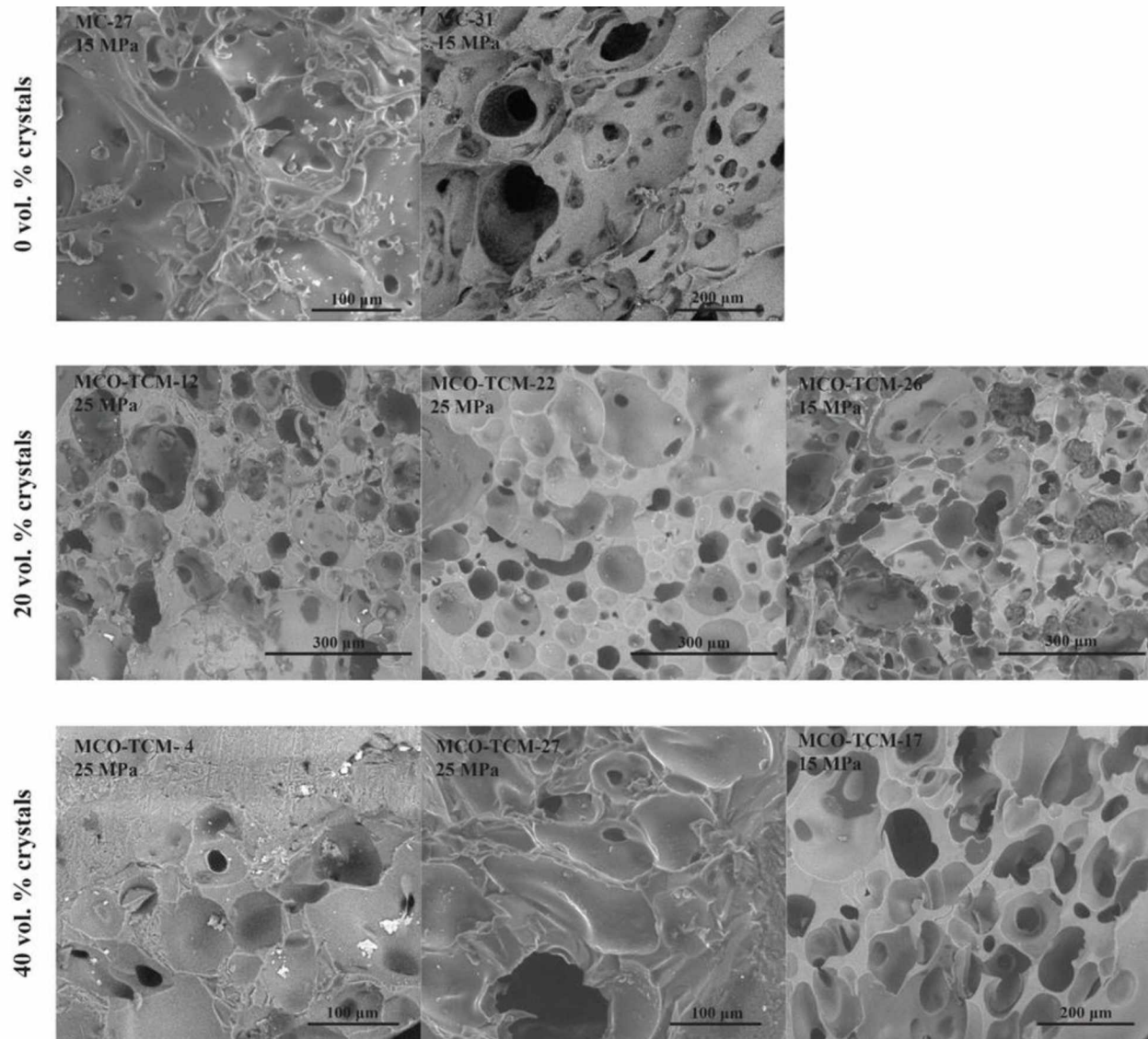
Figure 9. Selected BSE images from each sample imaged. Corundum does not show a different brightness than surrounding glass, but has a far different texture, as seen in the image representing MCO-TCM-4. Smaller bright particles are Fe-Ti oxides, and larger bright particles are remnant polishing compound grains. Individual scale bars for each image are displayed.

pore throat radius also generally increases with increasing permeability. The minimum pore throat measurements range from 2.0-3.2 μm in the 20 vol. % crystals series and from 2.5-4.0 μm in the 40 vol. % crystals series. The maximum pore throat measurements range from 34.4-41.9 μm in the 20 vol. % crystals series and from 26.9-58.1 μm in the 40 vol. % crystals series (Table 5). The 40 vol. % crystals series appears to have larger minimum pore throat measurements, but the trend in the maximum pore throat measurements is less clear. A set of the BSE images

captured from each sample is shown in Figure 9. One important thing to note in the BSE images is the presence of Fe-Ti oxides but in a proportion less than 1 vol. %.

Table 5. Pore throat measurement summary

Sample	Number	Average Radius (μm)	Minimum Radius (μm)	Maximum Radius (μm)	Median Radius (μm)
MCO-TCM-12	99	10.48	2	35.19	8.72
MCO-TCM-22	91	10.16	2.26	41.87	7.83
MCO-TCM-4	25	10.16	2.47	26.88	8.14
MCO-TCM-27	54	7.27	1.54	20.36	7.11
MC-27	159	8.63	0.92	106.49	6.07
MC-31	84	16.38	2.07	123.521	10.88
MCO-TCM-26	110	12.02	3.2	34.36	11.42
MCO-TCM-17	43	17.05	3.97	58.07	14.84

4.3 Dissolved water content

Micro-FTIR analyses of dissolved water were collected on five samples - 25 MPa P_f, 30 MPa P_f, two 50 MPa P_f, and 110 MPa P_f (Table 6). Since both crystal series appeared to follow equilibrium degassing and had similar porosities at the same quench pressures, it was assumed that the water contents should be similar between the two series as well. Sample thickness measurements showed good consistency at each point, with a standard deviation of <2 μm at each specific point. MCO-NEQ-6 (P_f = 110 MPa; Table 4) was used to assess whether the samples were saturating completely during the 24 hour hold period. Five points were measured across the whole of the sample with an average water content of 3.9 ±0.3 wt. %, which is within error of the equilibrium solubility value calculated by Moore et al. (1998) of 4.15 wt. %. Only one sample (MCO-TCM-13; 40 vol. % crystals; P_f = 30 MPa) showed significant undersaturation with a measured water content of 1.4 ±0.2 wt. % compared to the equilibrium predicted value of 2.0 wt. % (Figure 10; Table 6). One issue discovered with these measurements
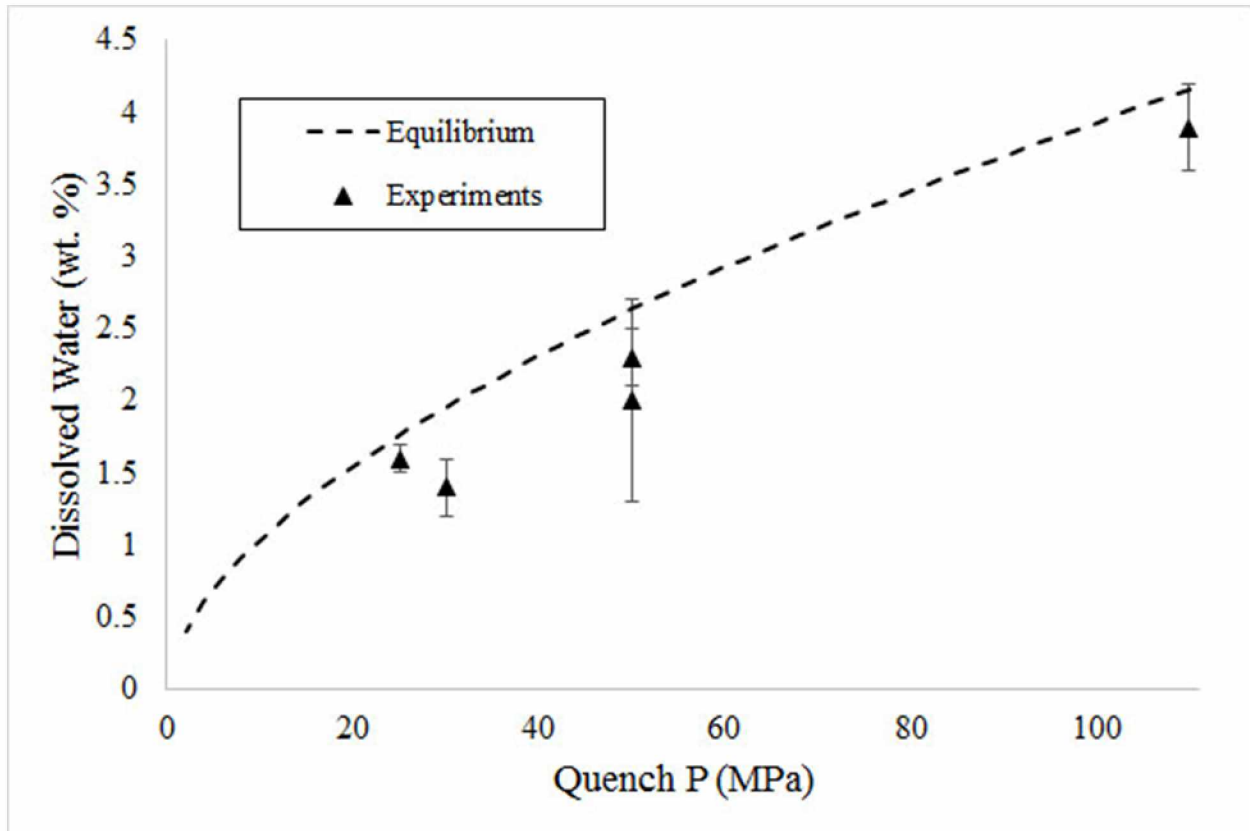
Figure 10. Dissolved water content versus quench pressure. Equilibrium water content is calculated using the equilibrium porosity equation from Gardner et al. (1999) and the water solubility model of Moore et al. (1998).

is that if the measurement is collected too close to a corundum seed crystal, the resulting water

content was far lower than other measurements. This is likely a result of the corundum proximity

changing the index of refraction slightly and thus changing the estimation of the thickness. The

measured undersaturation for MCO-TCM-13 is likely a result of one or more points having been

collected too close to a corundum seed crystal.

5.0 Discussion

    5.1 Experimental porosities, hydration bubbles, and bubble nucleation

    According to the experimental method, bubble nucleation likely occurred prior to the

main decompression, introducing a population of small bubbles during the hold period before

decompression. The experiments were pressurized to 90 MPa then allowed to equilibrate in

Table 6. Summary of FTIR measurements

Sample	Measurement	Thickness (μm)[a]	A_{3570}	A_{4500}	A_{5230}	Total Water (wt. %)
MCO-NEQ-6	1	56.4 (1.0)		0.016 (0.001)	0.026 (0.001)	3.62
	2	63.8 (0.8)		0.020 (0.001)	0.035 (0.001)	4.19
	3	82.5 (1.2)		0.026 (0.001)	0.043 (0.002)	4.05
	4	60.3 (0.2)		0.016 (0.001)	0.030 (0.001)	3.70
	Avg					3.89 (0.3)
MCO-TCM-2	1	79.8 (2.1)		0.021 (0.001)	0.021 (0.001)	2.58
	2	42.2 (0.3)	1.016 (0.005)			2.13
	3	33.3 (0.1)	0.868 (0.003)			2.31
	4	31.4 (0.3)	0.716 (0.002)			2.02
	Avg					2.26 (0.2)
MCO-TCM-6	1	67.5 (0.2)		0.012 (0.001)	0.018 (0.001)	2.21
	2	52.6 (0.4)		0.009 (0.001)	0.009 (0.001)	1.61
	3	70.8 (1.7)		0.013 (0.000)	0.008 (0.001)	1.87
	4	70.3 (1.1)		0.011 (0.001)	0.007 (0.001)	1.23
	5	36.1 (0.5)		0.012 (0.001)	0.011 (0.001)	3.15
	Avg					2.02 (0.7)
MCO-TCM-13	1	48.8 (0.3)	0.795 (0.004)			1.43
	2	42.9 (0.9)	0.776 (0.003)			1.59
	3	45.4 (0.6)	0.682 (0.003)			1.32
	4	46.6 (1.4)	0.582 (0.001)			1.10
	Avg					1.36 (0.2)
MCO-TCM-20	1	76.6 (0.9)	1.218 (0.015)			1.39
	2	63.6 (1.3)	1.243 (0.010)			1.71
	3	56.0 (0.8)	0.981 (0.006)			1.53
	4	76.2 (0.8)	1.448 (0.016)			1.67
	Avg					1.58 (0.1)

[a] Numbers in parentheses are the 1σ standard deviations

temperature with the furnace. Heating the vessel caused gas expansion, so by the end of the temperature equilibration the pressure typically rose to around 120 MPa. The extra 10 MPa was bled off, and the experiment held for 24 hours from that point. However, as seen in the BSE and tomography images (Figures 9 and 11, respectively), some Fe-Ti oxides are present in the

experiments. It only takes a decompression of 5 MPa to nucleate bubbles on these oxides, so likely some nucleation occurred during that small decompression (Hurwitz and Navon, 1994).
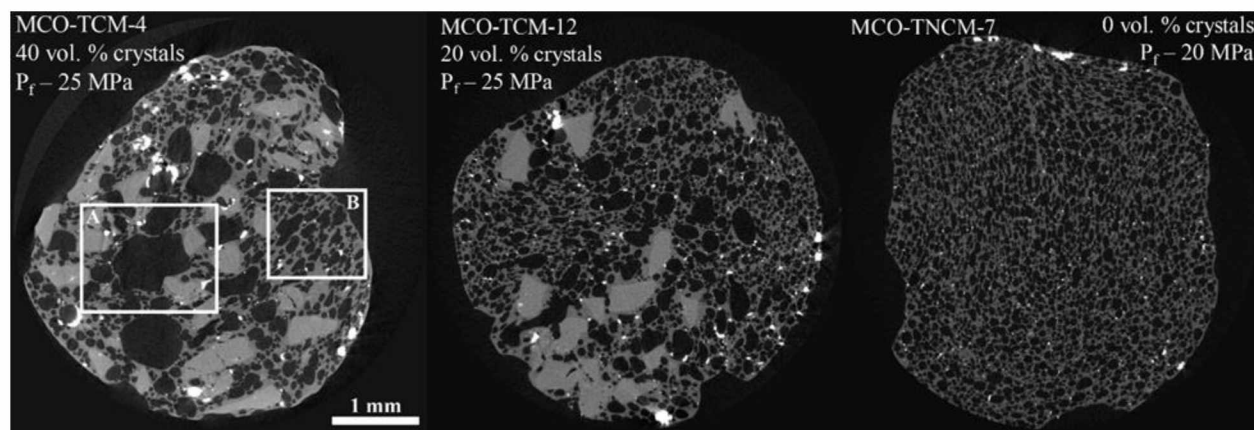
Figure 11. Selected tomography slices. Block A is an area where bubbles are larger due to coalescence and Block B is an area where bubbles are smaller due to less coalescence. Corundum crystals are the lighter grey, glass is the darker grey, and void spaces are black. The brighter spots are likely Fe-Ti oxides. The scale is the same for all three images.

As described previously, the powder starting material introduced hydration bubbles before the experiments were decompressed. Thus, growth of the hydration bubbles likely occurred during the initial decompression to bring the experiments to their desired hold pressure of 110 MPa. Since the rhyolites are so viscous, the 24-hour hold period is unlikely to be long enough for the bubbles to completely collapse and resorb. The initial hydration and nucleated bubbles can be seen in the bubble size distribution plots (Figure 7). The highest quench pressure samples in each crystal series show a distribution that is shifted to the right relative to the next lowest quench pressure sample. At higher quench pressures, the peak of the distribution should be shifted to the left as bubble nucleation is the dominant process and produces smaller bubbles. However, this pattern is not seen because hydration bubbles tend to be much larger than nucleated bubbles during the early stages of the decompression process, thus shifting the peak to the right. Once the growth rate of the main decompression-induced bubbles has caught up to the hydration bubbles, the bubble size distributions show the expected patterns.

Hydration bubbles were unlikely to influence the permeability results reported here. Lindoo et al. (2016) ran experiments with both powdered and solid slab starting materials and noted no difference between the two in terms of permeability results. Solid slabs were not an option as starting materials for this study since the phenocryst content of the experiments needed to be strictly controlled, and that could only be achieved by seeding the experiments manually. However, since this study was concerned with processes occurring after the hydration bubbles were no longer an influence, they were an acceptable factor. The affected porosity measurements (e.g., experiments with $P_f \geq 50$ MPa) could be corrected, as was demonstrated (Figure 6).

Both melt and bulk viscosities were approximated for each experiment. Melt viscosity (η_o) was calculated from the model of Giordano et al. (2008), and bulk viscosity (η) was calculated using the Einstein-Roscoe equation:

$$\eta = \eta_o \left(1 - \frac{\Phi}{\Phi_m}\right)^{-n} \tag{8}$$

where Φ is the fraction of particles, Φ_m is the maximum close packing threshold, and n is a power-law constant. For these calculations, Φ was the vol. % crystals that were present in the specific experiment, and the common values of $\Phi_m = 0.6$ and n = 2 were used as constants. The approximated viscosity values were used in later model calculations.

5.2 Experiments as a representation of nature

An important consideration with experiments is whether they accurately model what happens in nature. Corundum has been determined to be a good analogue to typical phenocrysts found in rhyolites (e.g., quartz and feldspars). Typical phenocrysts found in rhyolite magmas, like plagioclase, are poor nucleation sites with acute wetting angles (Hurwitz and Navon, 1994;

Gardner et al., 2000), so the corundum should also be a poor nucleation site in rhyolites to ensure the results are not skewed by an artificial nucleated bubble population. Wetting angles measured from tomography images of two samples yield values of 47°±10 (MCO-TCM-2, n=21) and 45°±8 (MCO-TCM-6, n=18). An example of one measured wetting angle is shown in Figure 12. The acute values indicate that the melt wets the crystals strongly and thus nucleation is not favored. These values also agree well with the 46°±14 angles measured on corundum from Okumura et al. (2012). Thus, using corundum as the phenocryst did not skew the results by promoting nucleation.
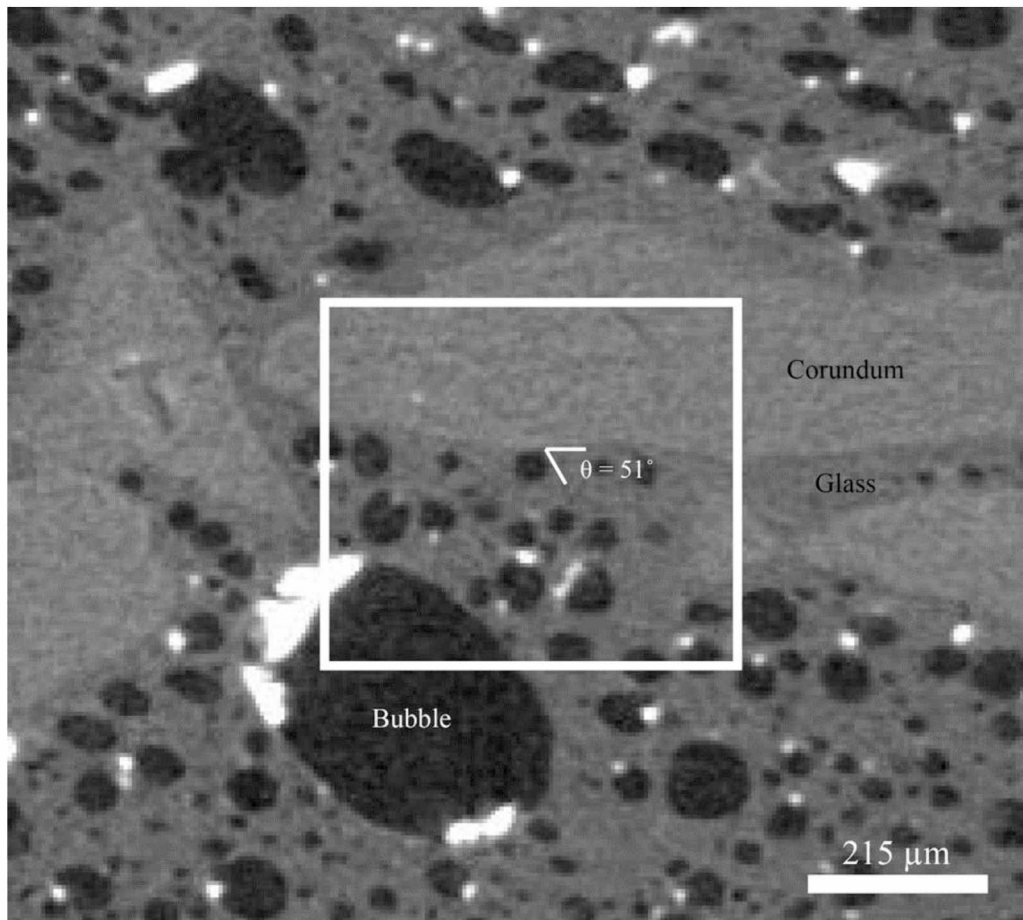
Figure 12. Example of measured bubble wetting angle on a corundum crystal. Image comes from a tomography slice, so the greyscale scheme is the same as described in Figure 11.

Another indication that the experiments can be applied to natural systems is the pore throat radii measurements. The maximum pore throat radii of the permeable experiments agree well with measurements from natural samples from Yokoyama and Takeuchi (2009; Figure 13). However, their porosimiter analyses could only measure the largest pore throat although permeability is dependent upon the smallest pore throat.

The measured k_2/k_1 ratios (Equation 4) of the experimental samples also match well with the measured k_2/k_1 ratios in natural samples (Figure 14). This ratio has been used to indicate whether experiments can be scaled up to apply to nature despite their smaller size (e.g., Rust and Cashman, 2004; Lindoo et al., 2016). Inertial permeability has been suggested to be more
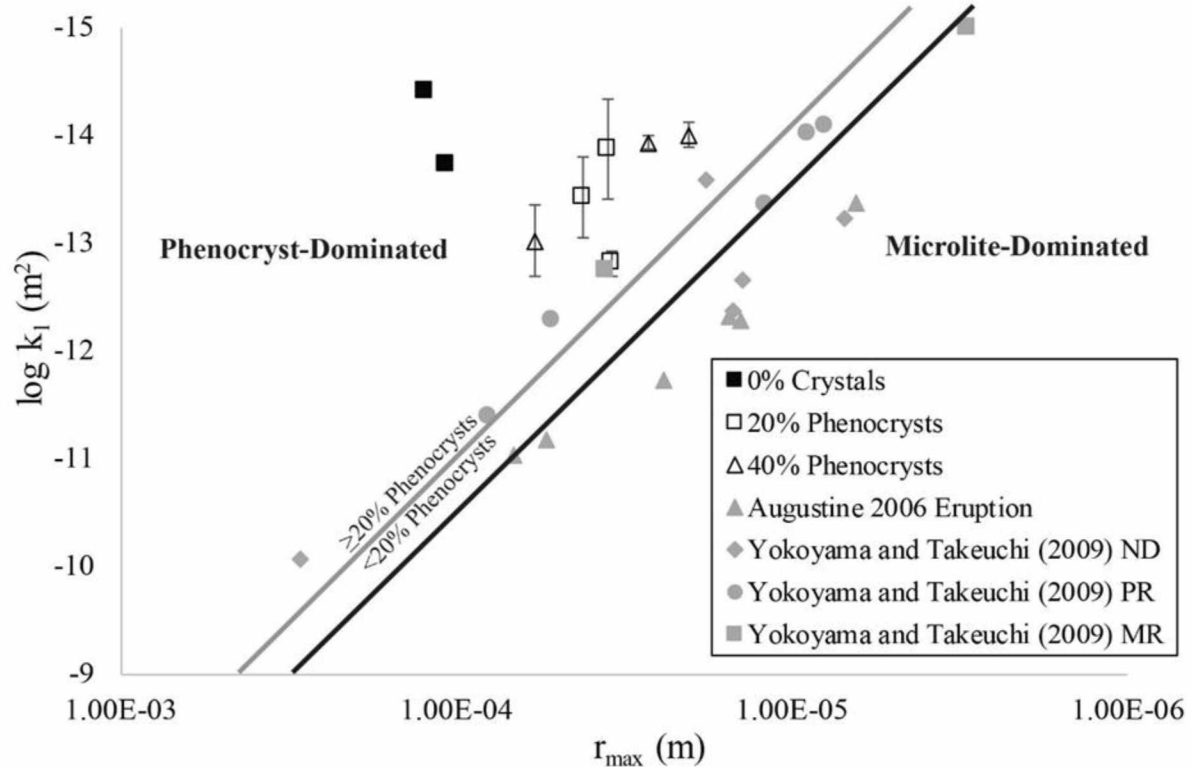
Figure 13. Plot of Darcian permeability versus maximum pore throat radius. Solid black line indicates the division between microlite-dominated and phenocryst-dominated fields. Solid grey line indicates the division between phenocryst contents within the phenocryst-dominated field. ND = no crystal content data, PR = phenocryst-rich, MR = microlite-rich.

sensitive to changes in pore structure due to the typically larger variation in order of magnitude (Rust and Cashman, 2004). As the tortuosity, or curviness, of the hydraulic pathways increase, inertial permeability will decrease (Rust and Cashman, 2004). In order to scale this effect with the overall permeability of the sample, the k_2/k_1 ratio is used and in natural samples has a power-law relationship (Rust and Cashman, 2004; Lindoo et al., 2016). Since this ratio follows the natural trend in the experiments, the hydraulic pathways developed in the experimental samples should be similar to what would be found in nature.

One aspect that the experiments cannot capture is large-scale features, such as bubbles larger than 2-3 mm in diameter. Coarsely vesicular material can be observed in natural effusive rhyolitic features, such as Obsidian Dome in the Inyo Domes complex, CA. This material has
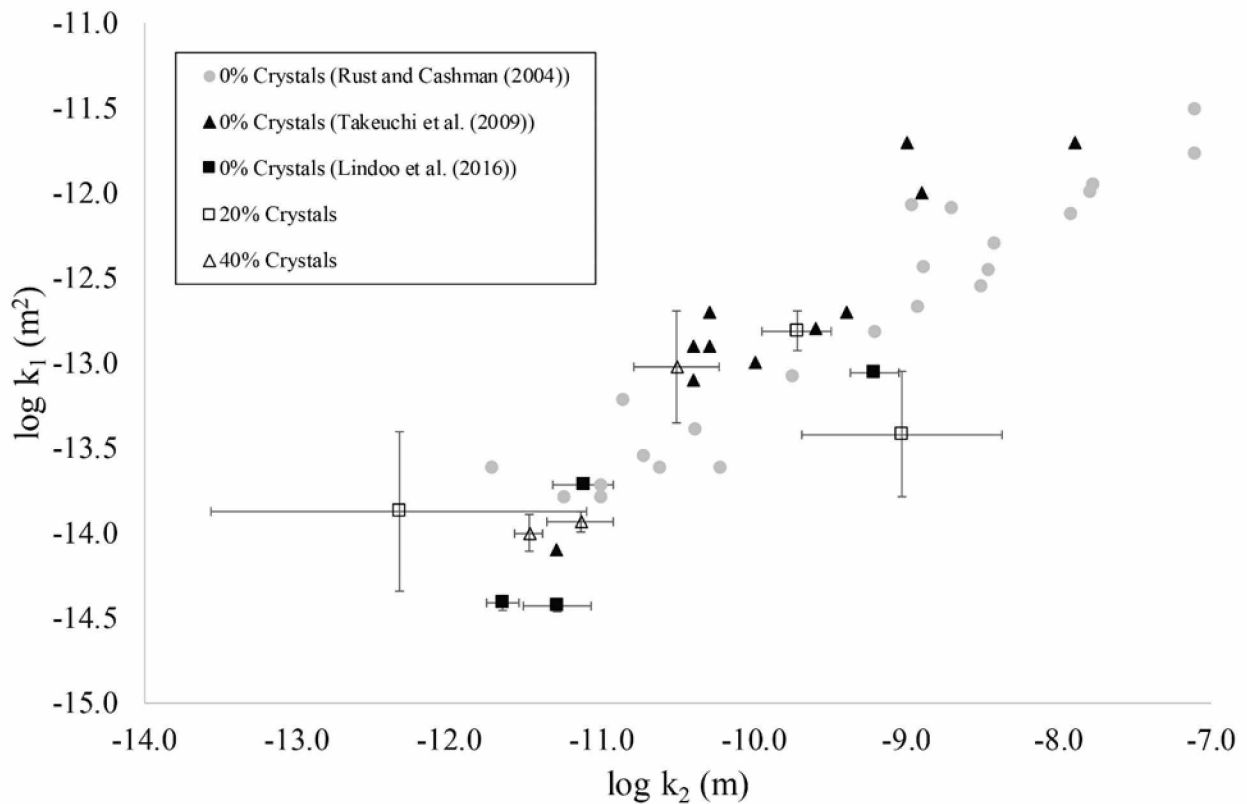

Figure 14. Plot of Darcian versus inertial permeability. Light grey markers indicate natural samples, solid black markers indicate other experimental samples, and open symbols indicate experiments from this study.

bubbles as large as several centimeters in diameter, which far surpasses the scope of what can be represented in the small experimental samples. However, lower quench pressure samples (≤ 25 MPa) with 40 vol. % phenocrysts have shown the start of larger bubbles (~3 mm diameter), so these larger-scale features seem to start developing in high-crystallinity systems at low pressures. Since these features seem to develop after permeability, they likely do not play a significant role in gas escape, which is what this study is concerned with. More likely, the larger bubbles seen in Obsidian Dome are related to the diapir rise mechanism proposed by Fink (1983). Therefore, the larger bubbles seen in Obsidian Dome are less significant for hydraulic pathways. The k_1/k_2 ratio trend shows that the experiments follow a similar hydraulic pathway trend as natural samples, so the lack of larger-scale features does not appear to influence permeability development.

5.3 Permeability and porosity

The percolation threshold of these crystal-bearing samples appears to be a sharp threshold at ~55 vol. % vesicularity (Figure 15), which is a decrease of 15 vol. % from the crystal-free percolation threshold of 70 vol. % vesicularity. An experiment without measurable permeability had a porosity of 54.9 vol.% whereas an experiment with measurable permeability had a porosity of 56.3 vol.%. There does not appear to be a significant difference in percolation threshold between the 20 and 40 vol. % crystal series. The crystal-free experiments did not show measurable permeability, with a maximum porosity of 69.7 vol. % at a quench pressure of 20 MPa. This is consistent with the results from Lindoo et al. (2016).

The decrease in percolation threshold seen in the crystal-bearing samples is likely a result of the crystals inducing coalescence. As seen in the analogue experiments conducted by Oppenheimer et al. (2015), suspended particles behave rigidly and force the vesicles to grow in pathways between the particles. Bubbles nucleate and begin growing in free space, moving the
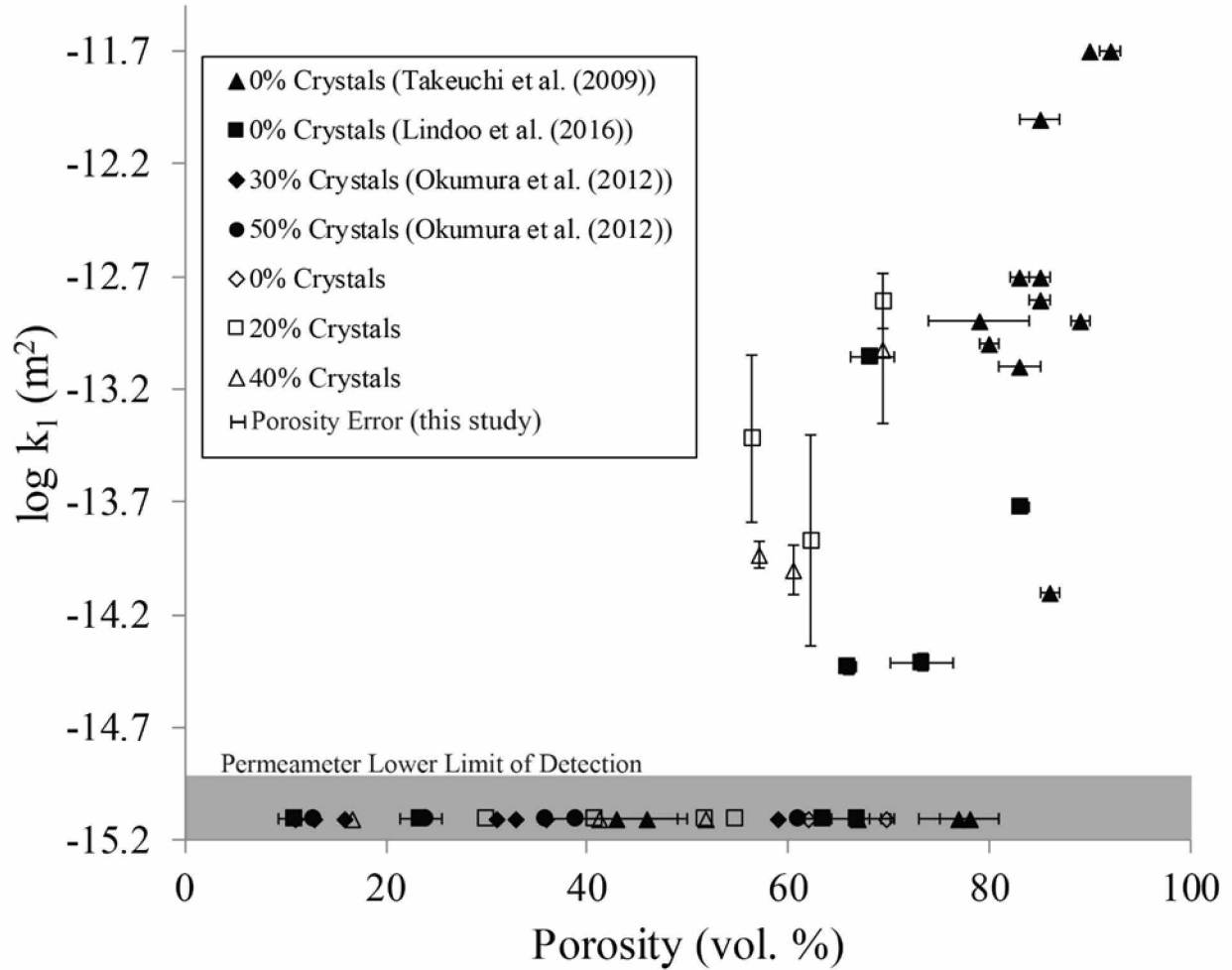
Figure 15. Percolation threshold of natural and experimental samples. Points plotted within the shaded area do not have permeability measurable by the laboratory permeameter (lower limit of detection: $\log k_1 = -15$). The error bars for the porosity measurement apply to all other porosity measurements from this study plotted in other figures.

melt out of the way. However, once the bubbles grow large enough to impinge on crystals, the bubbles do not have the force to move both the melt and the crystals. The bubbles will then be forced to expand into regions of the melt without crystals. If other bubbles are nearby, they will also be forced to grow into these crystal-free spaces. This will induce coalescence earlier on since the bubbles will impinge on one another much sooner than if they were allowed to grow freely in a radial direction (Figure 16). Evidence for this process can be seen qualitatively in the tomography images in Figure 11. The few larger bubbles that have almost certainly undergone coalescence tend to be concentrated between corundum crystals (Figure 11a), whereas crystal-free areas of the melt tend to have a larger proportion of smaller bubbles (Figure 11b). The

threshold at which the transition in bubble growth occurs appears to be ~20 vol. % crystals. At 20 vol. % crystals, the system is likely approaching a random loose packing arrangement where the crystals start to form a touching network (Oppenheimer et al., 2015). This touching network greatly increases the yield strength of the magma and makes it difficult for the bubbles to push the magma and crystals out of the way as they grow. The next rheological threshold would be at random close packing, which is likely above 40 vol. % particles, the maximum used in this study, since both the 20 and 40 vol. % series appear to behave the same.

The aspect ratios of the corundum seeds used in this study were quite low, with an average of 1.8 ±0.6. Since little work has been done to constrain the role of crystals in degassing, only the simplest case of low aspect ratio phenocrysts was considered in this study. However,
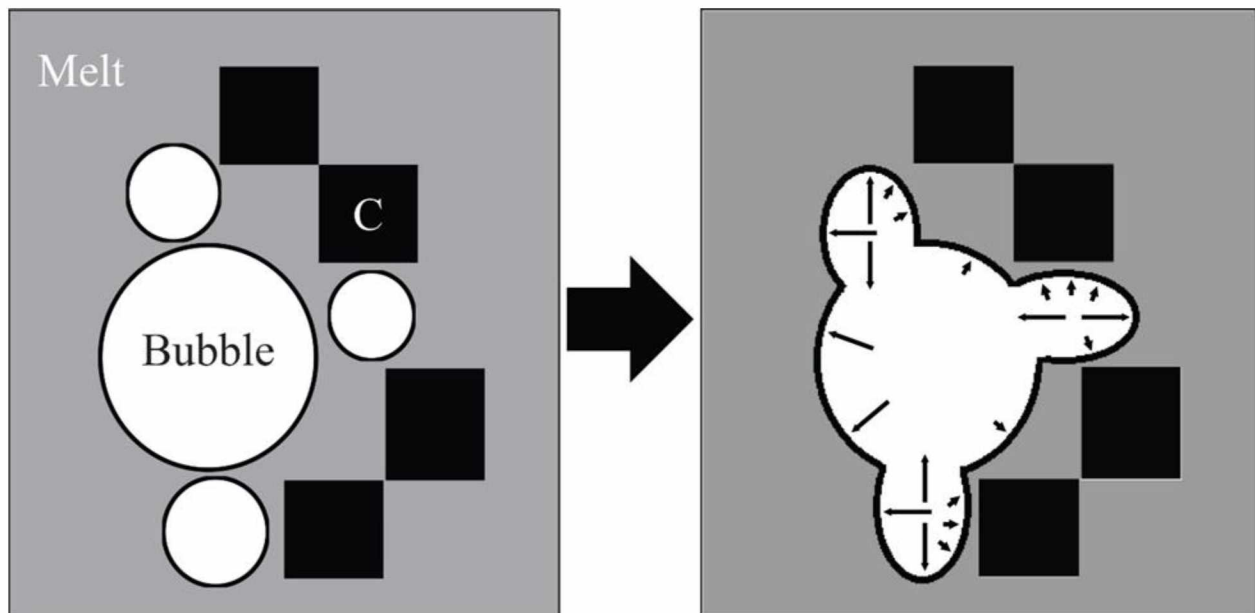
Figure 16. Schematic diagram showing bubble growth relative to phenocryst networks. The black squares with a "C" represent crystals. The length of the arrows on the right indicate magnitude of possible bubble growth in specific directions. Not to scale.

analogue experiments suggest that crystal shape influences the thresholds of random loose packing and random close packing (Mueller et al., 2011). As aspect ratio increases, the threshold for random loose packing will decrease, and the effects on porosity observed in these

experiments could occur at lower than the 20 vol. % crystals predicted at the low aspect ratios in this study (Mueller et al., 2011). For example, the presence of high aspect microlites could produce this effect.

The permeability results from this study differ from the results of Okumura et al. (2012). They reported no measured permeability even with phenocryst percentages up to 50 vol. % and measured vesicularities up to 61 vol. %. In contrast, this study measured permeability in both 20 and 40 vol. % phenocryst experiments with vesicularities as low as 56.3 and 57.1 vol. %, respectively. This difference can likely be explained by differences in experimental technique. Okumura et al. (2012) decompressed their samples by instantaneously dropping the pressure to the desired P_f then holding the experiment at that pressure for either 1 or 10 hours in order to allow the melt to come to equilibrium. In contrast, the experiments in this study were decompressed continuously at a constant rate then quenched within 10 seconds of reaching the desired P_f. The melt relaxation timescale is an important consideration with a longer hold time at P_f. This value describes how long it takes a deformed bubble to return to its original spherical shape and can be described with the equation from Toramaru (1995):

$$\tau_r \approx \frac{\eta R_{dec}}{\sigma} \tag{9}$$

where η is melt viscosity, R_{dec} is bubble equivalent radius, and σ is surface tension. Using values of $\eta = 2 \times 10^6$ Pa s from the melt viscosity at 25 MPa and $\sigma = 0.06$ N/m calculated for a hydrated rhyolite from Larsen and Gardner (2000) and a bubble radius of 50 μm as a representative bubble size from permeable sample MCO-TCM-12, a relaxation time scale of ≈27 minutes is obtained. Thus, even the shorter 1 hour hold time is more than twice the time needed for the bubbles to return to their original spherical shape. This could result in collapse of the pore apertures, which

then results in a lack of measurable permeability while still preserving the porosity. Lindoo et al. (2016) documented this phenomenon in low viscosity basaltic andesite experiments, in which they reported no measurable permeability in experiments with porosities up to 63 vol. %. However, their calculated melt relaxation time scale was 0.3 seconds, much faster than the possible quench time of 2-3 seconds. Thus, they concluded that the basaltic andesites must have become permeable, degassed, and then permeable pathways collapsed once the gas was no longer propping them open. Since the experiments in this study were quenched faster than the relaxation timescale, any permeability that developed during decompression was preserved.

5.4 Vesicle structure

The maximum pore throat radius versus permeability trend in these samples matches well with natural sample measurements from Yokoyama and Takeuchi (2009) and samples from the 2006 eruption of Augustine Volcano, Alaska (J. Larsen, unpublished data) despite differing methods of measurement (Figure 13). The natural samples were measured using porosimetry, which involved applying pressure to a water-saturated sample and noting at what pressure the first bubble of air was expelled, whereas the experiments were measured using images from one surface. It is possible the measurements reported for the experiments do not reflect the actual maximum or actual minimum pore throat radii since it is possible the one surface measured did not intersect that particular pore throat. However, since the measurements agree well both with natural samples and expected trends, it is unlikely that there is a large error associated with the differing method.

The experiments tend to have larger pore throat radii at a given k_1 value than the natural samples, particularly the crystal-free experiments. For example, at comparable log k_1 values, MC-27 (log k_1 = -13.7) has a maximum pore throat radius of 106.5 μm, MCO-TCM-22 (log k_1 =

-13.4) has a maximum pore throat radius of 41.9 μm, and a natural sample (log k_1 = -13.4) has a maximum pore throat radius of 12 μm (Table 5). Natural samples are not quenched as rapidly as the experiments, so there is a window of time after fragmentation when expansion, vesicle collapse, clast deformation on impact, and melt relaxation processes can influence vesicle structure. Depending on the initial size of the ejected pyroclast, melt relaxation and deformation may be more prevalent. Larger pyroclasts could have insulated centers that remain above the glass transition temperature for longer periods of time, allowing for more influence on vesicle structure from melt relaxation and deformation, thus resulting in smaller pore throats than were originally present at the time of fragmentation.

Another apparent control on pore throat radius is crystal content and crystal type (e.g., phenocrysts versus microlites; Figure 13). The Augustine samples have a significant amount of microlites, >50 vol. % except for one sample that only has 21 vol. %, and these samples along with all the microlite-rich samples from Yokoyama and Takeuchi (2009), except for one, have systematically smaller pore throats than the samples dominated by phenocrysts. Additionally, samples with ≥20 vol. % phenocrysts tend to have larger pore throats than samples with <20 vol. % phenocrysts. The presence of microlites seems to restrict the size of pore throats, whereas the presence of at least 20 vol. % phenocrysts seems to promote the formation of larger pore throats. Thus, it would be expected that a phenocryst-rich magma would be more permeable than a microlite-rich magma. This trend in pore throat size could be related to crystal packing and crystals restricting bubble growth. The pore throats in microlite-rich samples are likely smaller because the small microlites can pack closer together and thus restrict the size of the bubbles by decreasing the melt available for the bubbles to grow in. Analogue experiments conducted by Cimarelli et al. (2011) show that, in polydisperse crystal size distributions, increasing the fraction

of small prolate particles (e.g., microlites) increases the viscosity of a magma, likely as a result of the packing of the microlite-like particles. As discussed above, the bubbles cannot push crystals and melt out of the way while they are growing, particularly when the crystals are tightly packed together, thus the bubbles can only grow in areas of pure melt. Tightly packed microlites will restrict the available melt area, and bubbles will coalesce when they are much smaller, thus resulting in smaller pore throats. The difference between the two different phenocryst contents is similarly related to the random loose packing threshold. Having at least 20 vol. % phenocrysts was demonstrated earlier to induce more wide-spread coalescence, which likely also promotes larger pore throats relative to phenocryst-poor samples as well. Since none of the natural samples available are reported to be crystal-free, it is unclear whether the much larger pore throats seen in the two crystal-free experiments is also reflected in natural samples. However, the larger pore throats could be related to the fact that the bubbles in these experiments had to grow much larger before they coalesced, which would result in larger pore throats.

Disregarding the highest quench pressure distributions (discussed above), the distributions show the expected patterns based on shifts from bubble nucleation to bubble growth and coalescence. At the highest quench pressures, the 40 vol. % crystals series shows a distribution shifted more to the right than the 20 vol. % crystals series as well as bubbles in larger size divisions. Thus, the crystals appear to influence vesicle structure by increasing bubble size, likely by inducing coalescence. As seen in Figure 7, there is an obvious increase in bubble size with increasing crystal content at comparable quench pressures.

5.5 Implications for volcanic eruption style

Based on Figure 6 and the lack of supersaturation in FTIR measurements (Figure 10), the experiments degassed in equilibrium even at the fast decompression rate of 0.25 MPa/s.

Assuming a lithostatic pressure gradient of 23 MPa/km, this corresponds to an ascent rate of 9 m/s. This is an incredibly fast ascent rate to maintain equilibrium degassing, particularly for a rhyolite melt, and is contrary to results from Gardner et al. (1999). However, that study considered crystal-free rhyolites, so the presence of phenocrysts likely aided in maintaining equilibrium degassing even at the fast ascent rate. Thus, even at slower ascent rates, other crystal-rich magmas should also maintain equilibrium degassing, and the results from this study can be applied to these ascent rates.

Since the percolation threshold for magmas containing at least 20 vol. % phenocrysts shows a decrease by 15 vol. % porosity, the question remains whether this decrease in percolation threshold significantly affects magma degassing and transitions in eruption style in natural systems. The summary of this can be seen in Figure 17. The amount of water in wt. % that should still be within the system (M_t) after a period of water diffusing out is calculated from Zhang (1999):

$$M_t = M_o - M_o \sqrt{\frac{16D}{\pi L^2}} \sqrt{t} \qquad (10)$$

where M_o is the initial water wt. %, D is water diffusivity in cm^2/s, L is length in cm, and t is time in seconds. Water diffusivity is calculated from Nowak and Behrens (1997):

$$logD = (-4.81 - 0.045C + 0.027C^2) - \frac{(3378 - 483C + 46.9C^2 + 47.5P)}{T} \qquad (11)$$

where C is water concentration in wt. %, P is pressure in kbars, and T is temperature in K. The calculated water diffusivity (8.3×10^8 cm^2/s) used the pressure at which the crystal-bearing samples become permeable (25 MPa) and the M_o and C is the equilibrium water solubility at 25
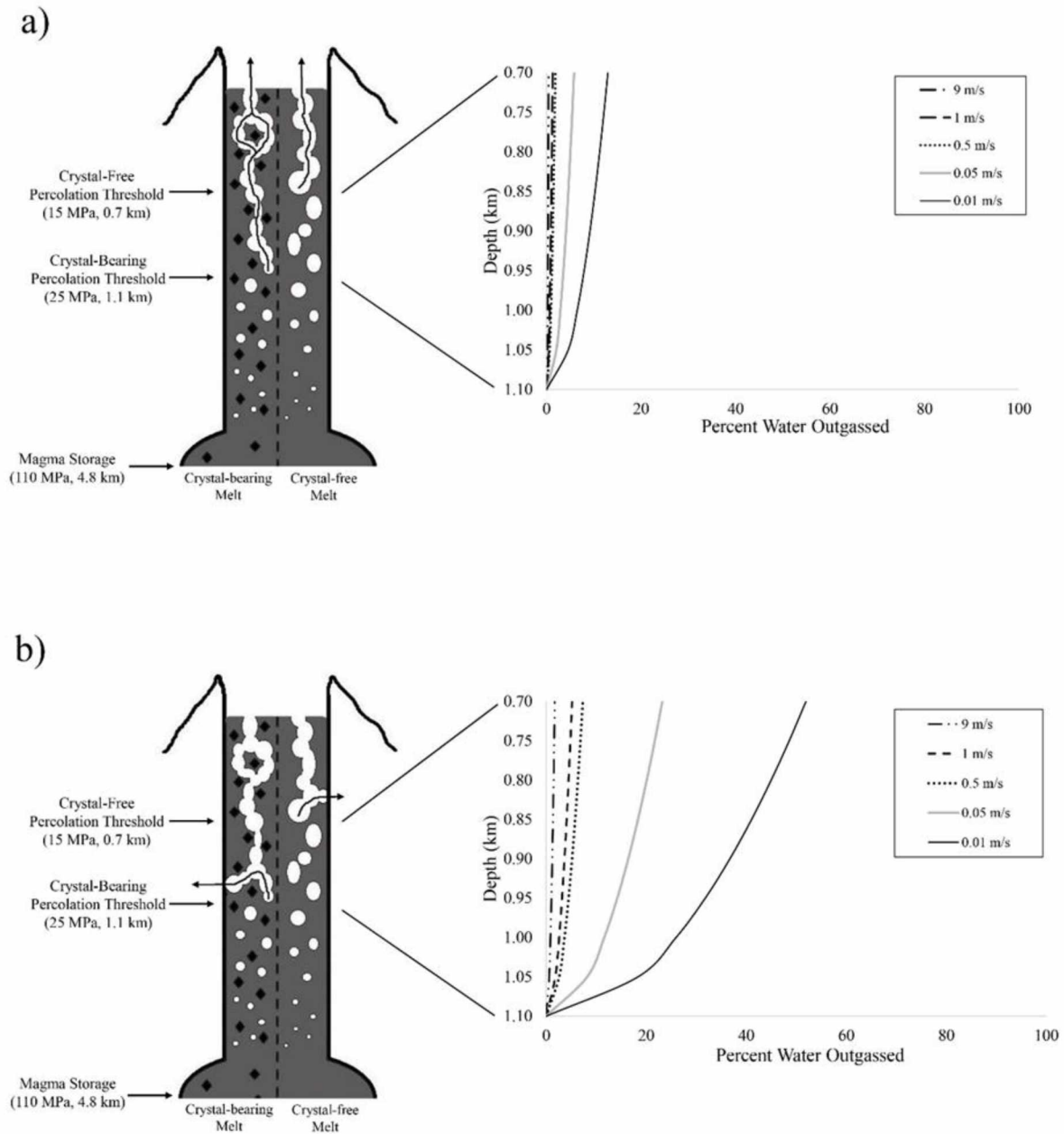
Figure 17. Conduit model of outgassing. The graphs represent the depths at which the crystal-bearing magma (left side of conduit) is permeable but the crystal-free magma (right side of conduit) is not. A) represents the case when only vertical outgassing is considered, and b) represents the case when only horizontal outgassing is considered. The conduit schematic is not to scale.

MPa (1.76 wt. %) based on the solubility model of Moore et al. (1998) for the Mono Craters

rhyolite. Only two methods of gas escape were considered – all gas escape is horizontal through

permeable conduit walls or all gas escape is vertical up the conduit through the permeable pathway. However, in real eruptions, a combination of gas escape directions is possible and the direction of gas escape can change over the course of an eruption, as discussed in the Background section. Another important assumption associated with this model is the rate of gas escape. This model assumes that all volatiles instantaneously escape as soon as they enter the permeable pathway. In contrast, there is likely a delay period between the time when the volatiles enter the permeable pathway and when the volatiles wholesale outgas from the magma. However, these complications present a modeling problem that is beyond the scope of this study, so the calculations presented are a first-order approximation of what is occurring in the conduit. Additionally, these calculations only model what is happening in a crystal-rich magma in the depth range where a crystal-rich magma would be permeable and a crystal-poor magma would not be permeable.

As seen in Figure 17, explosive ascent rate conditions (9 m/s and 1 m/s) do not allow for efficient gas escape, no matter which direction of gas loss is considered. At the most, these conditions show a loss of ~5% of the remaining water, which will not significantly change eruption style. However, at effusive ascent rates (0.5 m/s, 0.05 m/s, and 0.01 m/s), up to 50% of the remaining water can be lost, as long as the conduit walls are permeable. Thus, if a slowly ascending magma is crystal-rich, it could lose a significant portion of its water deep within the conduit. If it loses a large portion of its water deep within the conduit, that would decrease the amount of overpressure produced and will thus decrease the likelihood of fragmentation. However, if the conduit wall rocks are impermeable and all gas loss must be vertical, then only ~2-13% of the remaining water can be lost. These results imply that magma permeability, ascent rate, and permeability of the conduit wall all play an important role in determining gas escape.

The results of these experiments also have implications beyond rhyolitic systems. As dacitic and andesitic magmas crystallize, the matrix melt becomes increasingly silicic, and crystal-rich andesites have been shown to have rhyolitic matrix melt compositions (Martel and Iacono-Marziano, 2015). These conditions match the experiments in this study, with large crystal contents and rhyolite matrix melt, so the results from the experiments should be applicable to these systems as well. One of the more common explosive eruption styles seen in andesites is Vulcanian (e.g., Wright et al., 2012). These eruptions are characterized by gas-rich magma becoming trapped in the conduit below an impermeable lava plug and building pressure until the lava plug fails explosively. The typical yield strength of these lava plugs is 10-20 MPa (Wright et al., 2007).

In order to determine if the decrease in percolation threshold would relieve enough pressure in this situation, the amount of pressure bled off in the outgassing depth was calculated, only considering the pressure added to the bubbles during the outgassing period. The pressure within the bubbles can be estimated using the ideal gas law:

$$PV = nRT \qquad (12)$$

where P is pressure, V is volume, n is number of moles of gas, R is the ideal gas constant, and T is temperature. Since the experiments showed equilibrium porosity, the volume occupied by gas was calculated from the equilibrium porosity predicted at each depth. The number of moles of gas in the pores was calculated from the weight percent water that should have diffused into the bubbles (see above). Since the experiments were decompressed isothermally, this calculation also assumed an isothermal decompression at 900°C. The overpressure in the conduit was calculated by subtracting the lithostatic pressure from the calculated gas pressure (e.g., Diller et al., 2006).

45
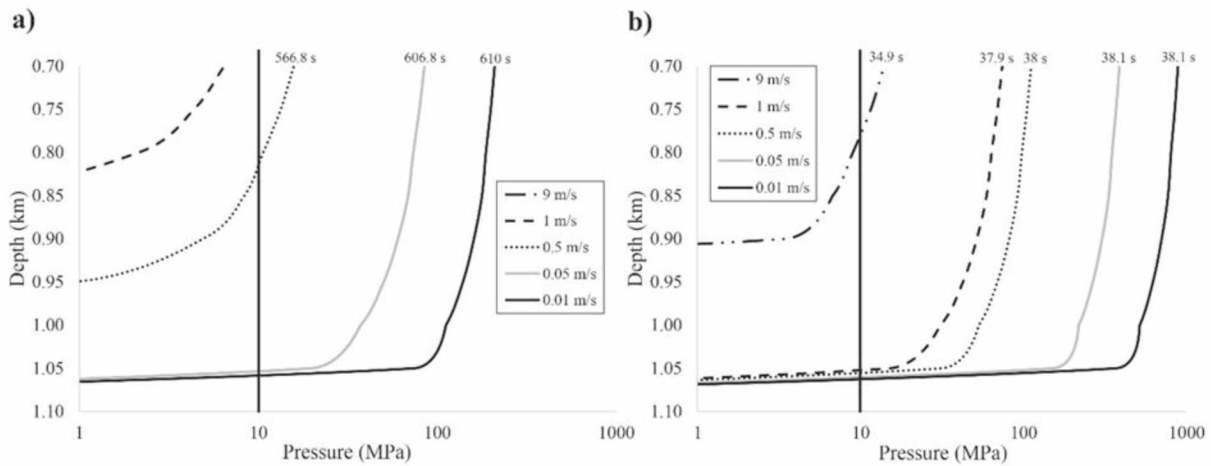
Figure 18. Gas pressure calculations relative to outgassing. Solid line represents 10 MPa threshold necessary for fragmenting an andesite lava plug. Times above the lines represent the time at which a magma would reach the 10 MPa threshold based on the various ascent rates. A) represents the case in which only vertical outgassing is considered, and b) represents the case in which only horizontal outgassing is considered.

In all cases considered, the timescale needed to dissipate at least 10 MPa is similar regardless of ascent rate, excluding cases where the conditions did not produce 10 MPa in gas pressure in the depth range considered (Figure 18). For example, in the vertical gas escape case, only the effusive ascent rates reach 10 MPa, but all three ascent rates reach this pressure threshold between 567-610 seconds. In the horizontal gas escape case, all five ascent rates reach the 10 MPa threshold between 35-38 seconds. Thus, ascent rate does not seem to affect the timescale of gas pressure escape but it does affect the depth at which it occurs. These results also confirm that horizontal gas escape is critical in dissipating gas pressure since the rate of gas escape is around 20x faster than in the vertical gas escape case.

These gas escape calculations can be placed in the context of Vulcanian eruption dynamics by comparison with a model of lava plug formation by Diller et al. (2006). This model considers lava plug formation as a function of gas escape direction, magma permeability

46

development, and ascent rate and was calibrated with data from the 1997 series of Vulcanian eruptions at Soufriere Hills volcano, Montserrat. A lava plug was only formed if a magma was permeable and all the gas could escape; the gas escape resulted in collapse of vesicles, thereby forming a dense lava plug. Their results produced three possible cases: 1) In the case of slower ascent rate and pure vertical gas escape, no lava plug was ever formed 2) In the case of slower ascent rate and allowing horizontal gas escape through permeable conduit walls, a lava plug formed, with thickness depending on depth of permeability development 3) In the case of rapid ascent rate and allowing horizontal gas escape, a lava plug is formed, though much thinner than any plug produced in Case 2. Case 2 was determined to be most applicable to the eruption of Soufriere Hills, but all three cases can be examined based on the calculations from this study. Important to note is the continued confirmation that horizontal gas escape is critical for producing effusive lava flows.

Case 1 is most relevant to the scenarios in which only vertical gas escape is considered. These explosive ascent rate scenarios in particular have very little gas loss in the 1.1-0.7 km depth range, which means it would be unlikely for the magma to completely degas and then collapse to form a lava plug in the remaining 700 m before the surface. In this case, if there was already a plug in place, the overpressure from the trapped gas would likely fragment the plug and produce a Vulcanian explosion. Case 2 is most relevant to all the ascent rates, except 9 m/s, where horizontal gas escape is considered. These scenarios have significant pressure dissipation relatively deep within the conduit (>1 km depth), so the likelihood that the magma will degas enough to produce collapse of vesicles and thus a lava plug is much higher. Case 3 is most relevant to the 9 m/s ascent rate where horizontal gas escape is considered. The magma still manages to lose a significant amount of pressure, but it occurs much shallower in the conduit

47

(~750 m) than the scenarios in Case 2. With the shallower degassing, a thinner lava plug should be formed based on the Diller et al. (2006) results.

Typical Vulcanian sequences, such as at Soufriere Hills, have explosions that last for a few minutes and then repose periods that last for hours (Diller et al., 2006). While the timescales of gas pressure dissipation calculated here cannot completely explain these times, they fit with observations. As long as the conduit wall rocks remain permeable, the gas should be able to escape fairly rapidly relative at all ascent rates considered here. Thus, a crystal-rich magma should continue to extrude effusively as a dome, as seen during repose periods. However, once the conduit walls become impermeable, such as through precipitation of quartz from all the water vapor escaping through the conduit walls (Edmonds et al., 2003), pressure dissipation is far less efficient in the vertical direction, particularly if an impermeable lava plug has built up at the mouth of the conduit. The pressure from the trapped gas will rapidly exceed the yield strength of an andesite plug, explosively blowing the plug out. During the explosive phase, the conduit walls will likely become permeable again, either from wall fracture or the precipitated quartz getting scraped out, and the ascending magma will again be able to lose gas pressure efficiently.

6.0 Conclusions

This study found that the presence of phenocrysts at a population of at least 20 vol. % results in a reduction of the percolation threshold from 70-80 vol. % porosity in a crystal-free rhyolite to 55 vol. % porosity. These results are consistent with experiments from Lindoo et al. (2015) and analogue experiments from Oppenheimer et al. (2015). The differing results of Okumura et al. (2012) can be explained by differences in experimental technique. The likely mechanism for this decrease in percolation threshold is phenocrysts inducing more widespread coalescence by forcing bubbles to grow in specific pathways, as predicted by the analogue

48

experiments of Oppenheimer et al. (2015). Phenocryst contents of ≥20 vol. % are rheologically significant for producing this effect because it takes around 20 vol. % phenocrysts for them to form a touching network, which makes it difficult for growing bubbles to push both the melt and crystals out of the way.

These results have implications for transitioning explosive-effusive eruptions, particularly in the context of Vulcanian eruptions. A crystal-rich magma, commonly seen in hydrous intermediate compositions, will become permeable and start to lose gas deeper within the conduit and earlier in the degassing process than a crystal-free magma. Calculations of the magnitude of gas loss show that there is a strong dependence on whether gas is capable of escaping through the conduit walls. If horizontal gas escape is not possible, the timescale for gas escape through the vertical permeable pathway is almost 20x slower. The transition between effusive and explosive phases of Vulcanian eruptions can be explained by changes in permeability of the conduit wall rocks. As long as the conduit walls are permeable, a crystal-rich magma should be able to lose enough gas from the decreased percolation threshold to form an effusive lava extrusion, the thickness of which is dependent on ascent rate. Once conditions change and the conduit walls are no longer permeable, gas escape is far less efficient and overpressures will quickly reach a magnitude that is capable of blowing out the lava plug formed during the effusive phase. Thus, the presence of phenocrysts within a highly silicic magma, along with ascent rate and permeability of conduit wall rocks, have an important impact on the degassing process and help control eruption style.

7.0 References

Behrens, H., Zhang, Y., & Xu, Z. (2004). H_2O diffusion in dacitic and andesitic melts. *Geochimica et Cosmochimica Acta, 68*(24), 5139-5150.

Blower, J. (2001). Factors controlling permeability–porosity relationships in magma. *Bulletin of Volcanology, 63*(7), 497-504.

Burgisser, A., & Gardner, J. E. 2004. Experimental constraints on degassing and permeability in volcanic conduit flow. *Bulletin of Volcanology, 67*(1), 42-56.

Caricchi, L., Pommier, A., Pistone, M., Castro, J., Burgisser, A., & Perugini, D. (2011). Strain-induced magma degassing: insights from simple-shear experiments on bubble bearing melts. *Bulletin of Volcanology, 73*(9), 1245-1257.

Cashman, K. V., & McConnell, S. (2005). Transitions from explosive to effusive activity–the summer 1980 eruptions of Mount St. Helens. *Bulletin of Volcanology, 68*, 57-75.

Cashman, K. V., & Sparks, R. S. J. (2013). How volcanoes work: A 25 year perspective. *Geological Society of America Bulletin, 125*(5-6), 664-690.

Castro, J. M., Burgisser, A., Schipper, C. I., & Mancini, S. (2012a). Mechanisms of bubble coalescence in silicic magmas. *Bulletin of Volcanology, 74*(10), 2339-2352.

Castro, J. M., Cordonnier, B., Tuffen, H., Tobin, M. J., Puskar, L., Martin, M. C., & Bechtel, H. A. (2012b). The role of melt-fracture degassing in defusing explosive rhyolite eruptions at volcán Chaitén. *Earth and Planetary Science Letters, 333*, 63-69.

Cimarelli, C., Costa, A., Mueller, S., & Mader, H. M. (2011). Rheology of magmas with bimodal crystal size and shape distributions: Insights from analog experiments. *Geochemistry, Geophysics, Geosystems, 12*(7).

Diller, K., Clarke, A. B., Voight, B., & Neri, A. (2006). Mechanisms of conduit plug formation: Implications for vulcanian explosions. *Geophysical Research Letters, 33*(20).

Edmonds, M., Oppenheimer, C., Pyle, D. M., Herd, R. A., & Thompson, G. (2003). SO_2 emissions from Soufrière Hills Volcano and their relationship to conduit permeability, hydrothermal interaction and degassing regime. *Journal of Volcanology and Geothermal Research, 124*(1), 23-43.

Eichelberger, J. C., Carrigan, C. R., Westrich, H. R., & Price, R. H. (1986). Non-explosive silicic volcanism. *Nature, 323*(6089), 598-602.

Fink, J. H. (1983). Structure and emplacement of a rhyolitic obsidian flow: Little Glass Mountain, Medicine Lake Highland, northern California. *Geological Society of America Bulletin, 94*(3), 362-380.

Gardner, J. E., Hilton, M., & Carroll, M. R. (1999). Experimental constraints on degassing of magma: isothermal bubble growth during continuous decompression from high pressure. *Earth and Planetary Science Letters, 168*(1), 201-218.

Gardner, J. E., Hilton, M., & Carroll, M. R. (2000). Bubble growth in highly viscous silicate melts during continuous decompression from high pressure. *Geochimica et Cosmochimica Acta, 64*(8), 1473-1483.

Giordano, D., Russell, J. K., & Dingwell, D. B. (2008). Viscosity of magmatic liquids: a model. *Earth and Planetary Science Letters, 271*(1), 123-134.

Hauri, E., Wang, J., Dixon, J. E., King, P. L., Mandeville, C., & Newman, S. (2002). SIMS analysis of volatiles in silicate glasses: 1. Calibration, matrix effects and comparisons with FTIR. *Chemical Geology, 183*(1), 99-114.

Heiken, G., Wohletz, K., & Eichelberger, J. (1988). Fracture fillings and intrusive pyroclasts, Inyo Domes, California. *Journal of Geophysical Research: Solid Earth, 93*(B5), 4335-4350.

Hess, K. U., & Dingwell, D. D. (1996). Viscosities of hydrous leucogranitic melts: A non-Arrhenian model. *American Mineralogist, 81*(9-10), 1297-1300.

Hurwitz, S., & Navon, O. (1994). Bubble nucleation in rhyolitic melts: Experiments at high pressure, temperature, and water content. *Earth and Planetary Science Letters, 122*(3-4), 267-280.

Jaupart, C., & Allegre, C. J. (1991). Gas content, eruption rate and instabilities of eruption regime in silicic volcanoes. *Earth and Planetary Science Letters, 102*(3-4), 413-429.

King, P. L., & Larsen, J. F. (2013). A micro-reflectance IR spectroscopy method for analyzing volatile species in basaltic, andesitic, phonolitic, and rhyolitic glasses. *American Mineralogist, 98*(7), 1162-1171.

Klug, C., & Cashman, K. V. (1996). Permeability development in vesiculating magmas: implications for fragmentation. *Bulletin of Volcanology, 58*(2), 87-100.

Klug, C., Cashman, K., & Bacon, C. (2002). Structure and physical characteristics of pumice from the climactic eruption of Mount Mazama (Crater Lake), Oregon. *Bulletin of Volcanology, 64*(7), 486-501.

Lange, R. L., & Carmichael, I. S. (1990). Thermodynamic properties of silicate liquids with emphasis on density, thermal expansion and compressibility. *Reviews in Mineralogy and Geochemistry, 24*(1), 25-64.

Larsen, J. F., & Gardner, J.E. (2000). Experimental constraints on bubble interactions in rhyolite melts: implications for vesicle size distributions. *Earth and Planetary Science Letters, 180*(1), 201-214.

Larsen, J. F., & Gardner, J. E. (2004). Experimental study of water degassing from phonolite melts: implications for volatile oversaturation during magmatic ascent. *Journal of Volcanology and Geothermal Research, 134*(1), 109-124.

Larsen, J. F., Denis, M. H., & Gardner, J.E. (2004). Experimental study of bubble coalescence in rhyolitic and phonolitic melts. *Geochimica et Cosmochimica Acta, 68*(2), 333-344.

Lindoo, A. N., Larsen, J. F., & Cashman, K. V. (2015, December). The affect of pre and syn-ascent crystallization on vesiculation kinetics and permeability development in low viscosity magmas. In *AGU Fall Meeting Abstracts.*

Lindoo, A. N., Larsen, J. F., Cashman, K. V., Dunn, A. L., & Neill, O. K. (2016). An experimental study of permeability development as a function of crystal-free melt viscosity. *Earth and Planetary Science Letters, 435*, 45-54.

Mangan, M. T., & Sisson, T. W. (2000). Delayed, disequilibrium degassing in rhyolite magma: decompression experiments and implications for explosive volcanism. *Earth and Planetary Science Letters, 183*(3), 441-455.

Mangan, M. T., Sisson, T. W., & Hankins, W. B. (2004). Decompression experiments identify kinetic controls on explosive silicic eruptions. *Geophysical Research Letters, 31*(8).

Martel, C., & Iacono-Marziano, G. (2015). Timescales of bubble coalescence, outgassing, and foam collapse in decompressed rhyolitic melts. *Earth and Planetary Science Letters, 412*, 173-185.

Moore, G., Vennemann, T., & Carmichael, I. S. E. (1998). An empirical model for the solubility of H_2O in magmas to 3 kilobars. *American Mineralogist, 83*(1), 36-42.

Mueller, S., Llewellin, E. W., & Mader, H. M. (2011). The effect of particle shape on suspension viscosity and implications for magmatic flows. *Geophysical Research Letters, 38*(13).

Nguyen, C. T., Gonnermann, H. M., Chen, Y., Huber, C., Maiorano, A. A., Gouldstone, A., & Dufek, J. (2013). Film drainage and the lifetime of bubbles. *Geochemistry, Geophysics, Geosystems, 14*(9), 3616-3631.

Nichols, A. R., & Wysoczanski, R. J. (2007). Using micro-FTIR spectroscopy to measure volatile contents in small and unexposed inclusions hosted in olivine crystals. *Chemical Geology, 242*(3), 371-384.

Nowak, M., & Behrens, H. (1997). An experimental investigation on diffusion of water in haplogranitic melts. *Contributions to Mineralogy and Petrology, 126*(4), 365-376.

Okumura, S., Nakamura, M., Nakano, T., Uesugi, K., & Tsuchiyama, A. (2012). Experimental constraints on permeable gas transport in crystalline silicic magmas. *Contributions to Mineralogy and Petrology, 164*(3), 493-504.

Okumura, S., Nakamura, M., Tsuchiyama, A., Nakano, T., & Uesugi, K. (2008). Evolution of bubble microstructure in sheared rhyolite: Formation of a channel-like bubble network. *Journal of Geophysical Research: Solid Earth, 113*(B7).

Okumura, S., & Nakashima, S. (2005). Molar absorptivities of OH and H_2O in rhyolitic glass at room temperature and at 400 600° C. *American Mineralogist, 90*(2-3), 441-447.

Oppenheimer, J., Rust, A. C., Cashman, K. V., & Sandnes, B. (2015). Gas migration regimes and outgassing in particle-rich suspensions. *Frontiers in Physics, 3*, 60.

Proussevitch, A. A., & Sahagian, D. L. (1998). Dynamics and energetics of bubble growth in magmas: analytical formulation and numerical modeling. *Journal of Geophysical Research: Solid Earth, 103*(B8), 18223-18251.

Russ, J. C. (1986). *Practical stereology*. Springer Science & Business Media.

Rust, A. C., & Cashman, K. V. (2004). Permeability of vesicular silicic magma: inertial and hysteresis effects. *Earth and Planetary Science Letters, 228*(1), 93-107.

Saar, M. O., & Manga, M. (1999). Permeability-porosity relationship in vesicular basalts. *Geophysical Research Letters, 26*(1), 111-114.

Sahimi, M. (1994). *Applications of percolation theory*. CRC Press.

Shea, T., Houghton, B. F., Gurioli, L., Cashman, K. V., Hammer, J. E., & Hobden, B. J. (2010). Textural studies of vesicles in volcanic rocks: an integrated methodology. *Journal of Volcanology and Geothermal Research, 190*(3), 271-289.

Takeuchi, S., Nakashima, S., & Tomiya, A. (2008). Permeability measurements of natural and experimental volcanic materials with a simple permeameter: toward an understanding of magmatic degassing processes. *Journal of Volcanology and Geothermal Research, 177*(2), 329-339.

Takeuchi, S., Tomiya, A., & Shinohara, H. (2009). Degassing conditions for permeable silicic magmas: Implications from decompression experiments with constant rates. *Earth and Planetary Science Letters, 283*(1), 101-110.

Tamic, N., Behrens, H., & Holtz, F. (2001). The solubility of H_2O and CO_2 in rhyolitic melts in equilibrium with a mixed CO_2–H_2O fluid phase. *Chemical Geology, 174*(1), 333-347.

Toramaru, A. (1995). Numerical study of nucleation and growth of bubbles in viscous magmas. *Journal of Geophysical Research: Solid Earth, 100*(B2), 1913-1931.

Vetere, F., Behrens, H., Holtz, F., & Neuville, D. R. (2006). Viscosity of andesitic melts—new experimental data and a revised calculation model. *Chemical Geology, 228*(4), 233-245.

Wright, H. M., Cashman, K. V., Gottesfeld, E. H., & Roberts, J. J. (2009). Pore structure of volcanic clasts: measurements of permeability and electrical conductivity. *Earth and Planetary Science Letters, 280*(1), 93-104.

Wright, H. M., Cashman, K. V., Mothes, P. A., Hall, M. L., Ruiz, A. G., & Le Pennec, J. L. (2012). Estimating rates of decompression from textures of erupted ash particles produced by 1999–2006 eruptions of Tungurahua volcano, Ecuador. *Geology, 40*(7), 619-622.

Wright, H. M., Cashman, K. V., Rosi, M., & Cioni, R. (2007). Breadcrust bombs as indicators of Vulcanian eruption dynamics at Guagua Pichincha volcano, Ecuador. *Bulletin of Volcanology, 69*(3), 281-300.

Wysoczanski, R., & Tani, K. (2006). Spectroscopic FTIR imaging of water species in silicic volcanic glasses and melt inclusions: an example from the Izu-Bonin arc. *Journal of Volcanology and Geothermal Research, 156*(3), 302-314.

Yokoyama, T., & Takeuchi, S. (2009). Porosimetry of vesicular volcanic products by a water-expulsion method and the relationship of pore characteristics to permeability. *Journal of Geophysical Research: Solid Earth, 114*(B2).

Zhang, Y. (1999). H_2O in rhyolitic glasses and melts: measurement, speciation, solubility, and diffusion. *Reviews of Geophysics, 37*(4), 493-516.

Zhang, Y., & Behrens, H. (2000). H_2O diffusion in rhyolitic melts and glasses. *Chemical Geology, 169*(1), 243-262.